UiO : University of Oslo

Christopher Lawrence

Extreme Wave Statistics of Surface Gravity Waves over Bathymetry

Thesis submitted for the degree of Philosophiae Doctor

Department of Mathematics
Faculty of Mathematics and Natural Sciences

2021

Series of dissertations submitted to the
Faculty of Mathematics and Natural Sciences, University of Oslo
No. 2469

ISSN 1501-7710

Cover: Hanne Baadsgaard Utigard.
Print production: Reprosentralen, University of Oslo.

To my mother

Preface

This thesis is submitted in partial fulfillment of the requirements for the degree of *Philosophiae Doctor* at the University of Oslo. The research presented here was conducted at the University of Oslo, under the supervision of Professor Karsten Trulsen and Dr. Odin Gramstad.

One experimental work was conducted at the Hydrodynamics Laboratory at University of Oslo, studying the wave kinematics of regular waves propagating over a shoal. The experimental result was then compared with the numerical simulation.

The thesis is a collection of three papers and one report, presented in chronological order of writing. The papers are preceded by an introductory chapter that relates them to each other and provides background information and motivation for the work. I am the first author of all papers, and carried out all of the numerical simulations and the analysis.

Acknowledgements

The research presented in this dissertation has been carried out over the past 3 years in the Mechanics section, Department of Mathematics, University of Oslo. I am very grateful for the research opportunities offered by University of Oslo.

First and foremost, I deeply appreciate the support and guidance from my supervisor Prof. Karsten Trulsen. I enjoyed our discussions on extreme wave statistics and i am thankful for the continuous support.

I also would like to express my sincere gratitude to my co-supervisor Dr. Odin Gramstad for the attentive guidance. I am really thankful for his willingness to teach me nonlinear waves.

I greatly appreciate Olav for the assistance during my experimental work, Terje and Lucy for the assistance to run my simulation in the computer cluster. Many thanks go to my friends for their support during this research.

I am grateful to my family especially my brothers: Albert and Teguh for their support. I am trully grateful to my late father, Suyanto Tan, and my mother, Susanti Wijaya for their unconditional love, prayer and support. I thank Yemima for her love, patience and support. Finally, I thank God for all the blessings.

Christopher Lawrence
Oslo, November 2021

List of Papers

Paper I

C. Lawrence, O. Gramstad, and K. Trulsen "Variational Boussinesq model for kinematics calculation of surface gravity waves over bathymetry". In: *Wave Motion* **100** (2021), 102665. DOI: 10.1016/j.wavemoti.2020.102665.

Paper II

C. Lawrence, K. Trulsen, and O. Gramstad "Statistical properties of wave kinematics in long-crested irregular waves propagating over non-uniform bathymetry". In: *Physics of Fluid* **33** (2021), 046601. DOI: 10.1063/5.0047643.

Paper III

C. Lawrence, K. Trulsen, and O. Gramstad "Extreme wave statistics of surface elevation and velocity field of gravity waves over a two-dimensional bathymetry". To be submitted.

Paper IV

C. Lawrence "Embedded wave generation for surface gravity waves in a periodic domain". In preparation.

Contents

List of Figures

Chapter 1

Introduction

Ocean waves are fascinating to see but can be very dangerous. Freak ocean waves, also known as rogue waves, are unexpected and unusually larger waves than their surrounding. This phenomenon was introduced to the scientific community by Draper [1964]. The first scientific evidence of rogue waves was captured by a measuring instrument on January 1^{st} 1995 in the North sea at the Draupner platform. The instrument recorded a rogue wave with wave height of 25.6 m where the significant wave height in the area was around 12 m. The peak elevation above the still water level was 18.5 m. Figure 1.1 shows the 20 minutes record of the surface elevation from the Draupner platform. There is no unique definition of rogue waves. The most common criteria are suggested by Haver [2000]: within a 20 minutes time series,

$$\frac{H}{H_s} > 2 \quad \text{and/or} \quad \frac{\eta_{max}}{H_s} > 1.25, \tag{1.1}$$

the event is a possible rogue wave event. H is the distance from trough to crest, η_{max} is the distance from still water level to crest and H_s is the significant wave height. From this criteria, the Draupner wave can be categorized as a rogue wave event since its wave height is twice larger than the significant wave height.

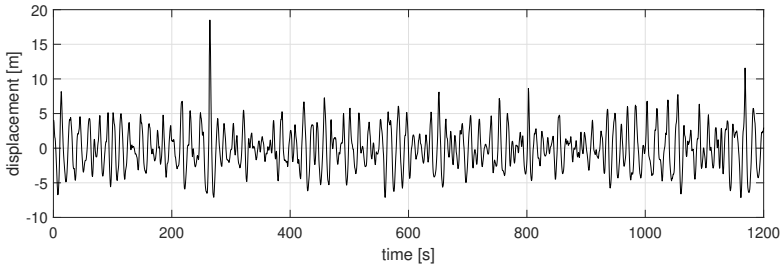

Figure 1.1: The full time series of the Draupner wave, recorded at the Draupner platform on January 1^{st}, 1995 at 15.20 GMT.

In the elementary model, ocean waves are modeled by linear superposition of a large number of independent wave components. This concept is illustrated in Figure 1.2 taken from Pierson et al. [1955]. By applying Central Limit Theorem, the wave fields follow Gaussian distribution or known as Gaussian sea. Rogue waves may occur within Gaussian seas, but such events are very rare. For example, the Draupner platform was designed to survive a 1-in-10000 years wave with a predicted wave height of 20 m. In fact, an extremely rare event with a wave height of 25.6 m was occurred and could give catastrophic

damage. Fortunately, there was no substantial damage and only minor damage was reported. Since then, the rogue waves topic gained huge interest in the scientific community.

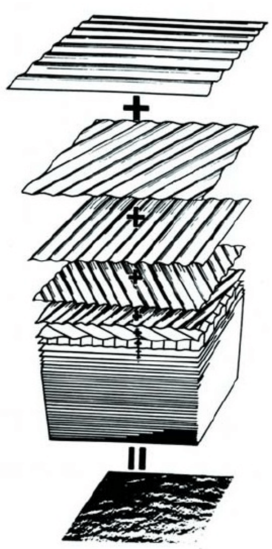

Figure 1.2: Linear superposition of independent wave components. Source: Pierson et al. [1955]

Rogue waves can be extremely dangerous for ships and offshore structures since it can impact directly to the structures and cause severe damage. Extreme weather has sunk hundreds of ships in the past decades and rogue waves are believed to be the major cause. The recent catalogues by Didenkulova [2020] compiled the occurrence of rogue waves reported in mass media and scientific literature during 2011-2018. Previously, Didenkulova et al. [2006], Liu [2007] and Nikolkina and Didenkulova [2011] also presented a collection of rogue wave events. Apparently, rogue waves are not very rare and their probability of occurrence can be higher under some circumstances. Several possible physical mechanisms of rogue wave phenomenon are discussed in the review by Kharif and Pelinovsky [2003] and annual review by Dysthe et al. [2008]. Book by Kharif et al. [2008] covered study of rogue waves in the ocean by using fully nonlinear hydrodynamic numerical models and included the analysis of real rogue wave events.

Nonlinearity can modify the wave statistics that deviate from Gaussian since the wave components are not independent hence the Central Limit Theorem is invalid. The simplest indicators for deviation from Gaussian are the skewness and the kurtosis. For the Gaussian sea, the skewness and the kurtosis are 0 and 3, respectively. A slight deviation from Gaussian statistics was noticed in the second-order Stokes wave in deep water by Tayfun [1980].

In higher-order theory, modulational instability of nonlinear water waves is

one of the mechanisms for rogue wave occurrence. This instability is also known as Benjamin-Feir (BF) instability since Benjamin and Feir [1967] discovered the instability of Stokes waves on deep water in the laboratory wave tank. Alber [1978] showed that the BF instability is more pronounced in a narrow band wave field. When BF instability is present, deviation from Gaussian statistics is stronger which implies the population of rogue waves increases. For short-crested waves, Gramstad and Trulsen [2007] showed the effect of BF instability is reduced as the directionality increases.

Laboratory wave tank helps to understand better the theory of water waves. Following the instability by Benjamin and Feir [1967], the effect of modulational instability was pronounced in the experiment of bichromatic wave train in long wave tank by Stansberg [1995]. Initially, the linear theory and the standard Nonlinear Schrodinger Equation are unable to predict the wave evolution correctly but Trulsen and Stansberg [2001] modified the Nonlinear Schrodinger Equation to improve the model that can predicts both the evolution of individual wave crests and the modulation of the envelope. Toffoli et al. [2013] showed experimentally that an opposite current may affect the wave evolution to become modulationally unstable. Guyenne [2017] found numerically that co-propagating current has a stabilizing effect while a counter-propagating current promotes wave growth.

The field measurement of the Draupner wave attracted the scientific community to analyze and reproduce it in the laboratory experiment. Recreation of the Draupner wave in a wave tank has been made by Clauss and Klein [2011] in 1D propagation and later by McAllister et al. [2019] in multi-directional propagation.

Trulsen et al. [2012] showed laboratory evidence of rogue waves provoked by a sloping bottom. For relatively long unidirectional waves propagating over a sloping bottom, from deeper to shallower water, non-Gaussian statistics are detected with a local maximum of skewness and kurtosis of surface elevation near the edge of the shallower side of the slope. Numerical simulations reported by Sergeeva et al. [2011], Gramstad et al. [2013], Viotti and Dias [2014] confirmed the experimental results. However, Zeng and Trulsen [2012] did not find the same peak of skewness and kurtosis of surface elevation on the shallower side of the slope because their wave field belongs to the deeper regime and also the bottom slope is long and mild.

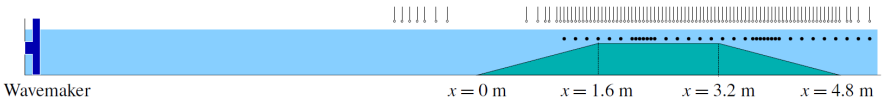

Figure 1.3: Layout of laboratory experiment of Trulsen with ultrasound probe and ADV measurement. Figure is taken from Trulsen et al. [2020].

Rogue waves not only occur in water waves, but also in other physical science such as optics. Extensive review of rogue waves in water waves and optics can be found in Dudley et al. [2019]. In oceanography, rogue waves are mostly connected with the surface elevation, but they actually exist in the other

quantities, for example velocity field. Trulsen et al. [2020] reported laboratory experiments of long-crested irregular waves propagating over a shoal (see Figure 1.3). They found a deviation from Gaussian statistics for both surface elevation and horizontal velocity field. Furthermore, the kurtosis of surface elevation and horizontal velocity is different. The peak kurtosis of surface velocity was found on top of the shoal but the peak kurtosis of horizontal velocity was located around the down slope of the shoal. Figure 1.4 shows the skewness and the kurtosis of surface elevation and horizontal velocity.

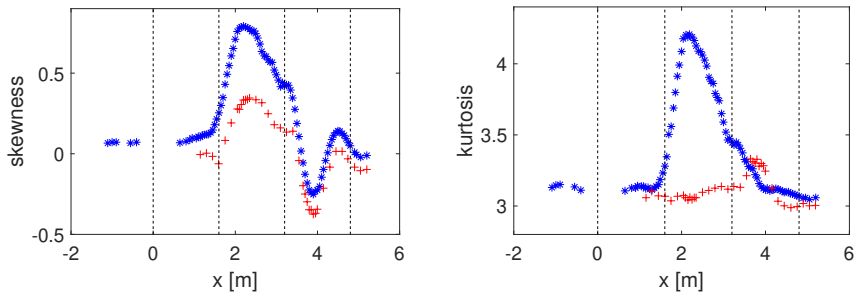

Figure 1.4: Skewness and kurtosis of surface elevation ($*$) and horizontal velocity ($+$) from laboratory experiment by Trulsen et al. [2020].

In the design of ships and offshore structures, estimating the wave-induced forces on the structures are essential. Morison et al. [1950] proposed a formula to estimate force on a body in an oscillatory flow, this formula has been widely used to estimate the wave loads in the design of offshore structures and known as the Morison equation. Horizontal velocity is involved directly in the Morison equation. High kurtosis in horizontal velocity implies higher probability of rogue wave occurrence in horizontal velocity. Hence, unexpected and unusually large wave loads may occur frequently. New findings from Trulsen et al. [2020] suggested that the kurtosis of surface elevation and horizontal velocity can have local maximum at different locations. It means that even though the surface elevation is strongly non-Gaussian but the horizontal velocity can be Gaussian and vice versa. The possibility to have high kurtosis in the horizontal velocity also suggests the best location of the offshore structures.

From these recent experiments, it is relevant to confirm the results by numerical simulation and extend the study for different bottom topography and wave fields. Accurate and reliable numerical simulation for nonlinear wave propagation over non-uniform bottom including the wave kinematics calculation is necessary.

1.1 Numerical method and validation

In this dissertation, nonlinear wave propagation model of High Order Spectral Method has been extensively used. The model was programmed carefully over

the years with validation cases. Brief summary of the method is presented in the following.

1.1.1 High Order Spectral Method

A 2D fluid domain, periodic in horizontal direction with length L and a Cartesian coordinate system is considered. Let $z = \eta(x,t)$ denote the free surface elevation with $z = 0$ is the still water level and $z = -h_0 + \mathcal{B}(x)$ the bottom topography where h_0 is the mean water depth and $\mathcal{B}(x)$ is the bottom variation. Figure 1.5 shows the sketch of computational domain.

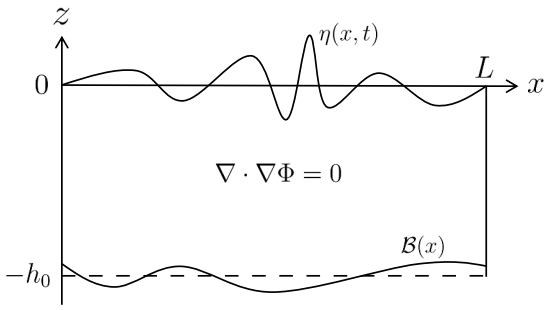

Figure 1.5: Sketch of computational domain with surface elevation $\eta(x,t)$, mean water depth h_0 and bottom variation $\mathcal{B}(x)$.

With the assumption of irrotational flow and incompressible fluid, the velocity potential Φ satisfies the Laplace equation $\nabla \cdot \nabla \phi = 0$. As pointed out in Zakharov [1968], the dynamic equations for inviscid irrotational nonlinear water waves satisfy Hamiltonian equations and can be written in terms of surface elevation $\eta(x,t)$ and surface potential $\phi_s = \phi(x, z = \eta, t)$

$$\begin{aligned} \frac{\partial \eta}{\partial t} &= W\left(1 + |\nabla \eta|^2\right) - \nabla \phi_s \cdot \nabla \eta \\ \frac{\partial \phi_s}{\partial t} &= -g\eta - \frac{1}{2}|\nabla \phi_s|^2 + \frac{1}{2}W^2\left(1 + |\nabla \eta|^2\right) \end{aligned} \tag{1.2}$$

where g is the acceleration of gravity and $W = \frac{\partial \phi}{\partial z}|_{z=\eta}$ is the vertical velocity at the surface. The surface vertical velocity W needs to be evaluated to solve the system (1.2). An efficient pseudo spectral method to calculate the surface vertical velocity W in terms of surface elevation η and surface potential ϕ_s was initially introduced by Dommermuth and Yue [1987] and West et al. [1987] for flat bottom, and has been known as High Order Spectral Method (HOSM). The extension of HOSM to include the bottom variation is discussed comprehensively in Gouin et al. [2016, 2017]. A brief summary of the High Order Spectral Method for varying bottom is presented in the following.

The velocity potential $\phi(x,z,t)$ and the surface vertical velocity $W(x,t)$ are expressed as a truncated power series

$$\begin{aligned}\phi(x,z,t) &= \sum_{m=1}^{M} \phi^{(m)}(x,z,t) \\ W(x,t) &= \sum_{m=1}^{M} W^{(m)}(x,t)\end{aligned} \tag{1.3}$$

where m denotes the nonlinear order of $\phi^{(m)}, W^{(m)}$ and M is the nonlinear order of the method which can be freely chosen. Then, using Taylor expansion around still water level $z=0$ on $\phi^{(m)}$ and $W^{(m)}$ gives

$$\begin{aligned}\phi^{(m)}(x,t) &= \sum_{n=0}^{m-1} \frac{\eta^n}{n!} \frac{\partial^n \phi^{(m)}}{\partial z^n}(x, z=0, t), \\ W^{(m)}(x,t) &= \sum_{n=0}^{m-1} \frac{\eta^n}{n!} \frac{\partial^{n+1} \phi^{(m)}}{\partial z^{n+1}}(x, z=0, t).\end{aligned} \tag{1.4}$$

From Equation (1.3) and (1.4), the surface potential ϕ_s can be expressed as

$$\phi_s(x,t) = \phi(x, z=\eta, t) = \sum_{m=1}^{M} \sum_{n=0}^{m-1} \frac{\eta^n}{n!} \frac{\partial^n \phi^{(m-n)}}{\partial z^n}(x, z=0, t). \tag{1.5}$$

Rewrite the left hand side and right hand side of Equation (1.5) according to the same order gives a triangular system:

$$\begin{aligned}
m=1, &\quad \phi_s = \phi^{(1)} \\
m=2, &\quad 0 = \eta \frac{\partial \phi^{(1)}}{\partial z} + \phi^{(2)} \\
m=3, &\quad 0 = \frac{\eta^2}{2!} \frac{\partial^2 \phi^{(1)}}{\partial z^2} + \eta \frac{\partial \phi^{(2)}}{\partial z} + \phi^{(3)} \\
m=4, &\quad 0 = \frac{\eta^3}{3!} \frac{\partial^3 \phi^{(1)}}{\partial z^3} + \frac{\eta^2}{2!} \frac{\partial^2 \phi^{(2)}}{\partial z^2} + \eta \frac{\partial \phi^{(3)}}{\partial z} + \phi^{(4)} \\
m=M, &\quad 0 = \sum_{n=0}^{M-1} \frac{\eta^n}{n!} \frac{\partial^n \phi^{(M-n)}}{\partial z^n}.
\end{aligned} \tag{1.6}$$

Rearrange Equation (1.6) gives the velocity potential solution at $z=0$ for each

order explicitly:

$$\begin{aligned}
\phi^{(1)} &= \phi_s \\
\phi^{(2)} &= -\eta \frac{\partial \phi^{(1)}}{\partial z} \\
\phi^{(3)} &= -\frac{\eta^2}{2!}\frac{\partial^2 \phi^{(1)}}{\partial z^2} - \eta \frac{\partial \phi^{(2)}}{\partial z} \\
\phi^{(4)} &= -\frac{\eta^3}{3!}\frac{\partial^3 \phi^{(1)}}{\partial z^3} - \frac{\eta^2}{2!}\frac{\partial^2 \phi^{(2)}}{\partial z^2} - \eta \frac{\partial \phi^{(3)}}{\partial z} \\
\phi^{(m)} &= -\sum_{n=1}^{m-1} \frac{\eta^n}{n!} \frac{\partial^n \phi^{(m-n)}}{\partial z^n}, \quad \text{for} \quad m > 1.
\end{aligned} \tag{1.7}$$

In the same way, the surface vertical velocity for each order $W^{(m)}$ is given as

$$\begin{aligned}
W^{(1)} &= \frac{\partial \phi^{(1)}}{\partial z} \\
W^{(2)} &= \eta \frac{\partial^2 \phi^{(1)}}{\partial z^2} + \frac{\partial \phi^{(2)}}{\partial z} \\
W^{(3)} &= \frac{\eta^2}{2!}\frac{\partial^3 \phi^{(1)}}{\partial z^3} + \eta \frac{\partial^2 \phi^{(2)}}{\partial z^2} + \frac{\partial \phi^{(3)}}{\partial z} \\
W^{(4)} &= \frac{\eta^3}{3!}\frac{\partial^4 \phi^{(1)}}{\partial z^4} + \frac{\eta^2}{2!}\frac{\partial^3 \phi^{(2)}}{\partial z^3} + \eta \frac{\partial^2 \phi^{(3)}}{\partial z^2} + \frac{\partial \phi^{(4)}}{\partial z} \\
W^{(m)} &= \sum_{n=0}^{m-1} \frac{\eta^n}{n!} \frac{\partial^{n+1} \phi^{(m-n)}}{\partial z^{n+1}}.
\end{aligned} \tag{1.8}$$

Dommermuth and Yue [1987] approximate the surface vertical velocity in the dynamic equations (1.2) with

$$\begin{aligned}
W\left(1 + |\nabla\eta|^2\right) &\approx \sum_{m=1}^{M} \left[W^{(m)} \left(1 + |\nabla\eta|^2\right) \right] \\
W^2\left(1 + |\nabla\eta|^2\right) &\approx \sum_{m=1}^{M} \left[\left(W^{(m)}\right)^2 \left(1 + |\nabla\eta|^2\right) \right].
\end{aligned} \tag{1.9}$$

Meanwhile, West et al. [1987] approximate these terms with consistent nonlinear order,

$$\begin{aligned}
W\left(1 + |\nabla\eta|^2\right) &\approx W^{(1)} + W^{(2)} + \sum_{m=3}^{M} \left(W^{(m)} + W^{(m-2)} |\nabla\eta|^2 \right) \\
W^2\left(1 + |\nabla\eta|^2\right) &\approx \sum_{m=2}^{M} \left(W^2\right)^{(m)} + \sum_{m=4}^{M} \left(W^2\right)^{(m-2)} |\nabla\eta|^2
\end{aligned} \tag{1.10}$$

with

$$\left(W^2\right)^{(m)} = \sum_{n=1}^{m} W_n W_{m-n}. \tag{1.11}$$

The latter method is preferred since it still maintain the Hamiltonian structure. For clarity, the dynamic equations of High Order Spectral Method based on West et al. [1987] up to fourth order are given as

$$\begin{aligned}\frac{\partial \eta}{\partial t} = &\quad W^{(1)} + \left(W^{(2)} - \nabla\phi_s \cdot \nabla\eta\right) \\ &+ \left(W^{(3)} + W^{(1)}\left|\nabla\eta\right|^2\right) + \left(W^{(4)} + W^{(2)}\left|\nabla\eta\right|^2\right) \\ \frac{\partial \phi_s}{\partial t} = &\quad -g\eta + \left(-\frac{1}{2}\left|\nabla\phi_s\right|^2 + \frac{W^{(1)}W^{(1)}}{2}\right) \\ &+ \left(W^{(1)}W^{(2)}\right) + \left(\frac{W^{(2)}W^{(2)} + 2W^{(1)}W^{(3)}}{2} + \frac{W^{(2)}W^{(2)}}{2}\left|\nabla\eta\right|^2\right).\end{aligned} \tag{1.12}$$

For varying bottom, the bottom boundary condition

$$\frac{\partial \phi}{\partial x}\frac{\partial \mathcal{B}}{\partial x} - \frac{\partial \phi}{\partial z} = 0 \quad \text{at} \quad z = -h_0 + \mathcal{B}(x), \tag{1.13}$$

needs to be satisfied. In order to satisfy the bottom boundary condition, an additional velocity potential ϕ_B is introduced and expressed as a truncated power series

$$\phi_B = \sum_{m=1}^{M} \phi_B^{(m)} \quad \text{and} \quad \phi_B^{(m)} = \sum_{l=1}^{M_B} \phi_B^{(m,l)} \tag{1.14}$$

where M_B is the nonlinear order for bottom boundary condition which can be different from M and can be freely chosen. Therefore, the velocity potential $\phi^{(m)}$ is expressed as the sum of two components

$$\begin{aligned}\phi^{(m)} &= \phi_0^{(m)} + \phi_B^{(m)}, \\ \phi_0^{(m)}(x,z,t) &= \sum_j A_j(t)\frac{\cosh k_j(z+h_0)}{\cosh k_j h_0}e^{ik_j x}, \\ \phi_B^{(m)}(x,z,t) &= \sum_j B_j(t)\frac{\sinh k_j z}{\cosh k_j h_0}e^{ik_j x},\end{aligned} \tag{1.15}$$

where $k_j = (j - \frac{N_x}{2} + 1)\frac{2\pi}{L}$ for $j = 0, \cdots, N_x - 1$. N_x is the number of wave components and it is chosen to be even number. A_j and B_j are the modal amplitudes of $\phi_0^{(m)}$ and $\phi_B^{(m)}$, respectively. With velocity potential in Equation (1.15) and bottom boundary condition in Equation (1.13), the modal amplitudes A_j and B_j can be calculated by using Taylor expansion of the bottom boundary condition around still water level $z = 0$ and truncate the series to order M_B. Once the modal amplitudes A_j and B_j have been known, the surface vertical velocity is calculated through Equation (1.8).

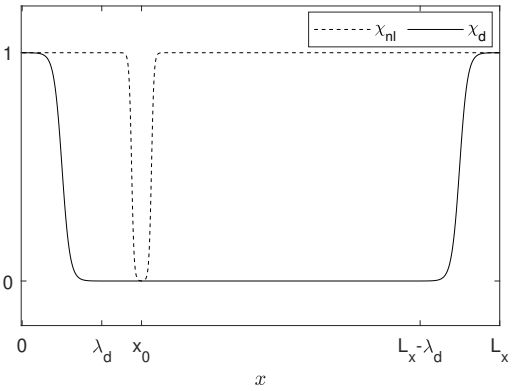

Figure 1.6: Smooth functions χ_d for damping zones (solid line) and χ_{nl} for spatial nonlinear adjustment (dashed line).

1.1.2 Wave generation and damping zones

Pseudo spectral method requires the boundary condition to be periodic. Therefore, the wave is generated inside the computational domain and damping zones are used to ensure the periodicity. Embedded wave generation is implemented with spatial nonlinear adjustment as discussed in Lie et al. [2014]. The dynamic equations of (1.2) become

$$\begin{aligned} \frac{\partial \eta}{\partial t} &= RHS_{lin} + RHS_{nonlin}\chi_{nl} - c_d\eta\chi_d + S_{x_0} \\ \frac{\partial \phi_s}{\partial t} &= RHS_{lin} + RHS_{nonlin}\chi_{nl} - c_d\phi_s\chi_d \end{aligned} \tag{1.16}$$

where RHS_{lin} and RHS_{nonlin} are the linear and nonlinear part of right hand side of the dynamic equations, c_d is the damping coefficient, S_{x_0} is the source term for wave generation at $x = x_0$, and χ_{nl}, χ_d are smooth functions for nonlinear adjustment and damping zones respectively. Illustration of the chosen functions for nonlinear adjustment and damping zones are shown in Figure 1.6.

1.1.3 Validation

Trulsen et al. [2020] reported laboratory experiments of irregular waves propagating over a shoal. Run 1 from Trulsen et al. [2020] is chosen as a test case to validate the numerical method. The experiment was conducted in the 24.6 m long and 0.5 m wide tank at the Hydrodynamic Laboratory of the Department of Mathematics at the University of Oslo. The wave is generated by wave maker at one end and absorbed at the other end by a damping beach. The shoal has 0.42 m height, 1.6 m of front slope and back slope and a horizontal section with length 1.6 m in the middle. The water depth is 0.5 m in the deeper region and 0.08 m on top of the shoal. The distance from wave maker to the tip of

the shoal is approximately 10.78 m. Surface elevation measurements were made with 16 ultrasound probes with distance of 0.3 m from each other. The wave probes can be moved along the tank. There were 4 sets of measurements: one before the shoal and three on top of the shoal. The sketch of the experimental setup is shown in Figure 1.7.

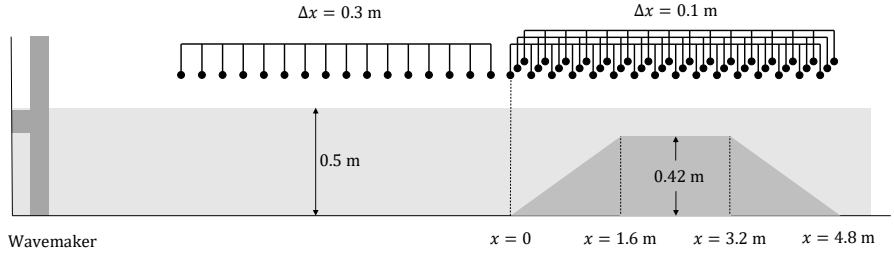

Figure 1.7: Sketch of laboratory experiment of run 1 from Trulsen et al. [2020].

High Order Spectral Method with $M = 3$ and $M_B = 10$ is employed for this case. The length of computational domain is 50 m and the length of damping zones are 15 m at both left and right boundaries. The wave generator is embedded in the domain at $x = -4.8$ m. The first wave probe closest to the wave maker is used for the wave generator in the simulation. The number of wave components is $N_x = 512$. Correlation coefficient and variance quotient between simulations and experiments are calculated as

$$\begin{aligned} corr &= \frac{cov(\eta_{sim}, \eta_{exp})}{\sigma_{\eta_{sim}} \sigma_{\eta_{exp}}} \\ varquo &= \frac{\sigma^2_{\eta_{sim}}}{\sigma^2_{\eta_{exp}}} \end{aligned} \tag{1.17}$$

where cov is the covariance and σ is the standard deviation. Figure 1.8 shows the correlation coefficient and variance quotient of surface elevation between simulation and experiment. Figure 1.9 shows the comparison of skewness and kurtosis of surface elevation between simulation and experiment. All of these quantitative information are calculated from sample $t \in [100, 860]$ s. Figure 1.10 and 1.11 show comparison of surface elevation between experiment and simulation at different locations.

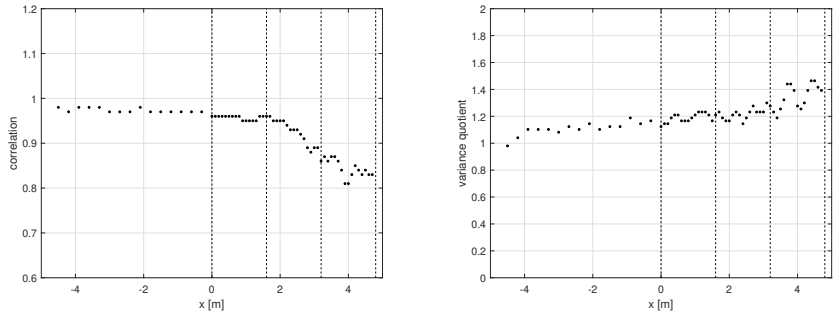

Figure 1.8: Correlation and variance quotient between simulation and experiment.

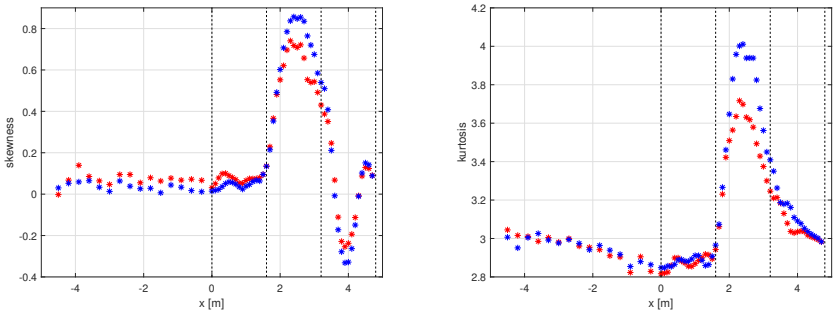

Figure 1.9: Skewness and kurtosis of surface elevation from experiment (blue, $*$) and simulation (red, $*$).

1.2 Present contributions

The dissertation is concerned with the non-Gaussian statistics of surface gravity waves provoked by non-uniform bathymetry. The main developments and findings in the papers are described in the following.

- Development of new numerical method for wave kinematics calculation from information of surface elevation and surface potential based on Variational Boussinesq model. The method is validated against Stokes waves, a solitary wave and laboratory experiment of regular waves over a shoal.

- Statistical study of surface elevation and horizontal velocity field of long-crested irregular waves over sloping bottom with different wave fields. The effects of significant wave height, peak period and bottom slope are discussed. Laboratory experiment by Trulsen et al. [2020] is confirmed in this work. In deeper regime, this work is the first verification of Zeng and Trulsen [2012] result.

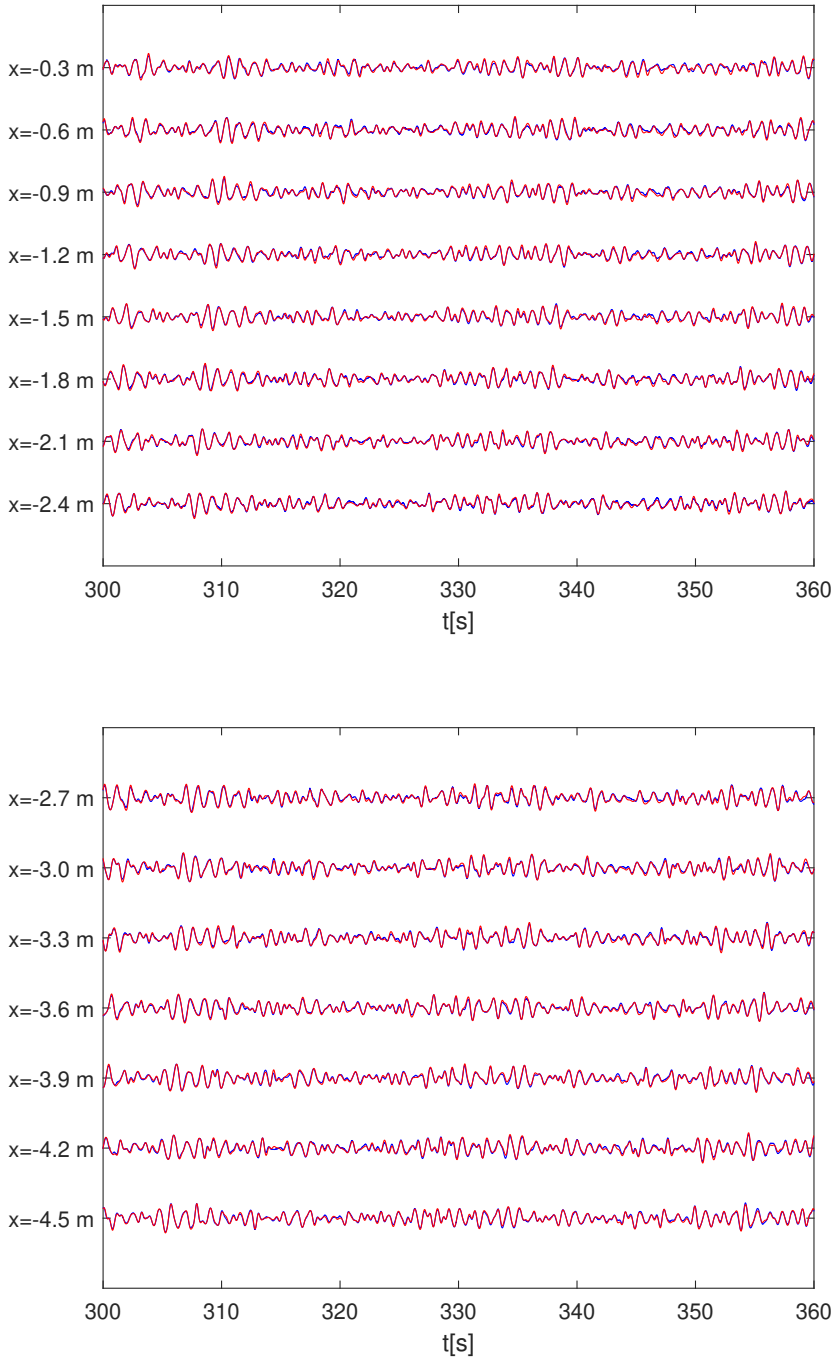

Figure 1.10: Surface elevation for the experiment (blue) and for the simulation (red) before the shoal.

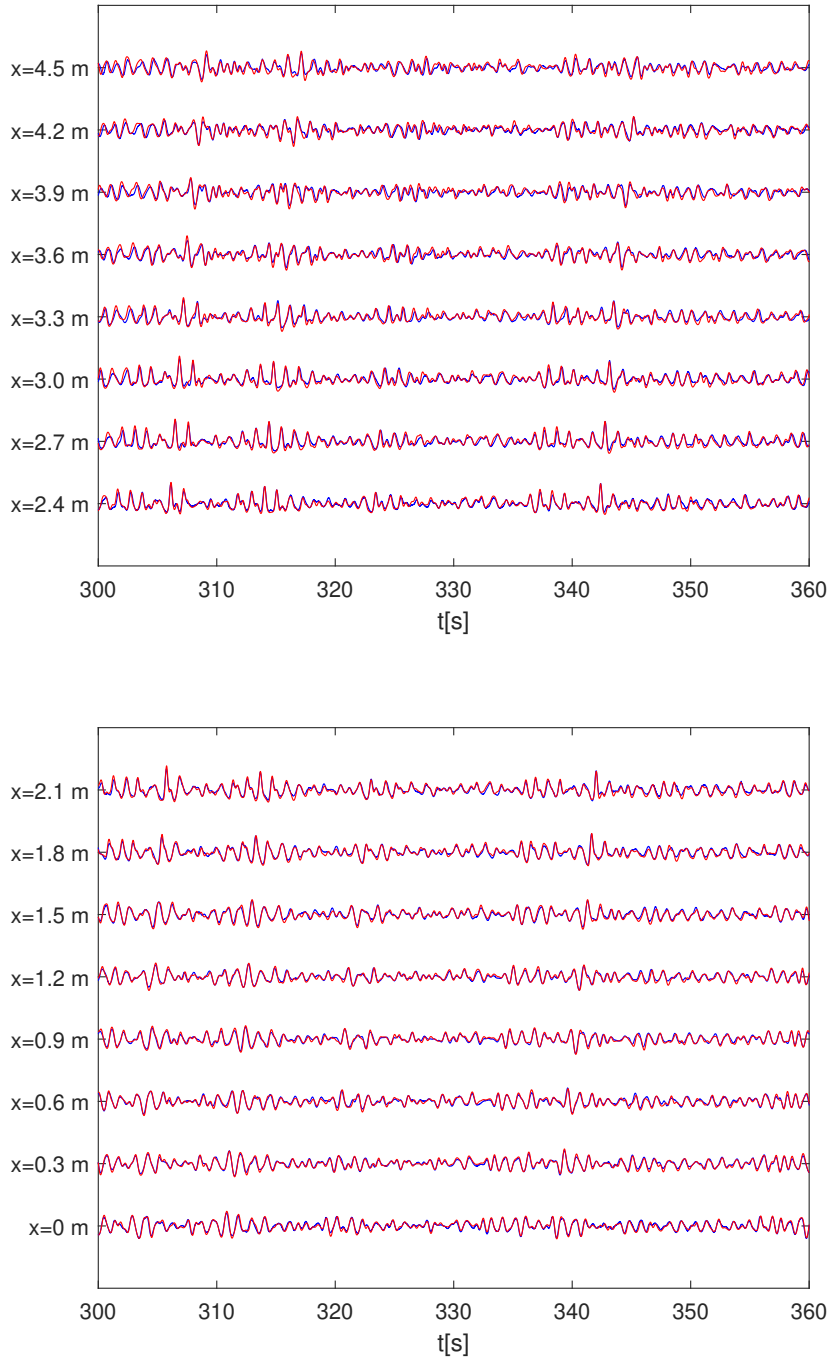

Figure 1.11: Surface elevation for the experiment (blue) and for the simulation (red) on top of the shoal.

- Statistical study of surface elevation and horizontal velocity field of long-crested irregular waves over a two-dimensional bathymetry. The refraction effect from the bathymetry can trigger non-Gaussian wave field. For long-crested irregular waves propagating over a circular shoal, the kurtosis of horizontal velocity field has two local maxima, different from the surface elevation. This finding implies that the rogue wave occurrence in the surface elevation and the horizontal velocity can be very different.
- Oblique wave generation is simulated and tested with waves propagating over an elliptic shoal on a slope. This work is the fundamental theory for multi-directional wave generation in the future work.

1.3 Summary of Papers

Paper I focuses on the numerical method for the calculation of wave kinematics from information about surface quantities and also wave kinematics measurement from laboratory experiment for the validation of the method.

Paper II presents the statistical properties of wave kinematics of long-crested irregular waves over varying bathymetry with various bottom slope and incoming waves.

Paper III investigates the statistical properties of surface elevation and velocity field of long-crested irregular waves propagating over a two-dimensional bathymetry.

Paper IV shows oblique wave generation in a periodic domain and its application on waves propagating over an elliptic shoal on a slope.

References

I. Alber. The effects of randomness on the stability of two-dimensional surface wavetrains. *Proc. R. Soc. Lond. A*, 363, 1978.

T. Benjamin and J. Feir. The disintegration of wavetrains on deep water. part 1. theory. *Journal of Fluid Mechanics*, 27:417–430, 1967.

G. Clauss and M. Klein. The new year wave in a seakeeping basin: generation, propagation, kinematics and dynamics. *Ocean Eng.*, 38:1624–1639, 2011.

E. Didenkulova. Catalogue of rogue waves occurred in the world ocean from 2011 to 2018 reported by mass media sources. *Ocean and Coastal Management*, 188:105076, 2020.

I. Didenkulova, A. Slunyaev, E. Pelinovsky, and C. Kharif. Freak waves in 2005. *Natural Hazards and Earth System Sciences*, 6:1007–1015, 2006.

D. G. Dommermuth and D. K. P. Yue. A high-order spectral method for the study of nonlinear gravity waves. *J. Fluid Mech.*, 184:267–288, 1987.

L. Draper. Freak ocean waves. *Oceanus*, pages 13–15, 1964.

J. Dudley, G. Genty, A. Mussot, A. Chabchoub, and F. Dias. Rogue waves and analogies in optics and oceanography. *Natural Review Physics*, 1:675–689, 2019.

K. Dysthe, H. E. Krogstad, and P. Muller. Oceanic rogue waves. *Annual review of Fluid Mechanics*, 40:287–310, 2008.

M. Gouin, G. Ducrozet, and P. Ferrant. Development and validation of a non-linear spectral model for water waves over variable depth. *European Journal of Mechanics - B/Fluids*, 57:115–128, 2016.

M. Gouin, G. Ducrozet, and P. Ferrant. Propagation of 3D nonlinear waves over an elliptical mound with a high-order spectral method. *European Journal of Mechanics - B/Fluids*, 63:9–24, 2017.

O. Gramstad and K. Trulsen. Influence of crest and group length on the occurrence of freak waves. *Journal of Fluid Mechanics*, 582:463–472, 2007.

O. Gramstad, H. Zeng, K. Trulsen, and G. K. Pedersen. Freak waves in weakly nonlinear unidirectional wave trains over a sloping bottom in shallow water. *Phys. Fluids*, 25(12), 2013.

P. Guyenne. A high-order spectral method for nonlinear water waves in the presence of a linear shear current. *Computer and Fluids*, 154:224–235, 2017.

S. Haver. Evidence of the existence of freak waves. In *In Rogue Waves 2000*, pages pp. 129–140. Ifremer, 2000.

C. Kharif and E. Pelinovsky. Physical mechanism of the rogue wave phenomenon. *European Journal of Mechanics - B*, 22:603–634, 2003.

C. Kharif, E. Pelinovsky, and E. Slunyaev. *A Rogue Waves in the Ocean*. Springer, 2008.

S. L. Lie, D. Adytia, and E. van Groesen. Embedded wave generation for dispersive surface wave models. *Ocean Engineering*, 80:73 – 83, 2014.

P. Liu. A chronology of freaque wave encounters. *Geofizika*, 24:57–70, 2007.

M. L. McAllister, S. Draycott, T. A. A. Adcock, P. H. Taylor, and T. S. van den Bremer. Laboratory recreation of the draupner wave and the role of breaking in crossing seas. *Journal of Fluid Mechanics*, 860:767–786, 2019.

J. Morison, M. O'Brien, J. Johnson, and S. Schaaf. The force exerted by surface waves on piles. *J. Petrol. Tech.*, 2:149–154, 1950.

I. Nikolkina and I. Didenkulova. Rogue waves in 2006-2010. *Natural Hazards and Earth System Sciences*, 11:2913–2924, 2011.

W. J. Pierson, G. Neumann, and R. W. James. *Practical methods for observing and forecasting ocean waves by means of wave spectra and statistics*. US Navy Hydrographic Office Pub. 603., 1955.

A. Sergeeva, E. Pelinovsky, and T. Talipova. Nonlinear random wave field in shallow water: variable Korteweg-de Vries framework. *Nat. Hazards Earth Syst. Sci.*, 11(2):323–330, Feb. 2011.

C. T. Stansberg. Spatially developing instabilities observed in experimental bichromatic wave trains. In *26th IAHR Congress (HYDRA 2000)*, volume 3, pages 180–185, 1995.

M. A. Tayfun. Narrow-band nonlinear sea waves. *J. Geophys. Res.*, 85:1548–1552, 1980.

A. Toffoli et al. Excitation of rogue waves in a variable medium: An experimental study on the interaction of water waves and currents. *Physical Review E*, 87: 051201(R), 2013.

K. Trulsen and C. T. Stansberg. Spatial evolution of water surface waves: Numerical simulation and experiment of bichromatic waves. In *International Offshore and Polar Engineering Conference*, 2001.

K. Trulsen, H. Zeng, and O. Gramstad. Laboratory evidence of freak waves provoked by non-uniform bathymetry. *Phys. Fluids*, 24(9):097101, 2012.

K. Trulsen, A. Raust∅l, S. Jorde, and L. B. Rye. Extreme wave statistics of long-crested irregular waves over a shoal. *Journal of Fluid Mechanics*, 882:R2, 2020.

C. Viotti and F. Dias. Extreme waves induced by strong depth transitions: Fully nonlinear results. *Physics of Fluids*, 26:051705, 2014.

B. J. West, K. A. Brueckner, R. S. Janda, D. M. Milder, and R. L. Milton. A new numerical method for surface hydrodynamics. *J. Geophys. Res.*, 92(C11): 11803–11824, 1987.

V. E. Zakharov. Stability of periodic waves of finite amplitude on the surface of a deep fluid. *J. Appl. Mech. Tech. Phys.*, 9:190–194, 1968.

H. Zeng and K. Trulsen. Evolution of skewness and kurtosis of weakly nonlinear unidirectional waves over a sloping bottom. *Natural Hazards and Earth System Sciences*, 12:631–638, 2012.

Papers

Paper I

Variational Boussinesq model for kinematics calculation of surface gravity waves over bathymetry

Christopher Lawrence, Odin Gramstad, Karsten Trulsen

Published in *Wave Motion* **100** (2021), 102665.
DOI: 10.1016/j.wavemoti.2020.102665.

Wave Motion 100 (2021) 102665

Contents lists available at ScienceDirect

Wave Motion

journal homepage: www.elsevier.com/locate/wamot

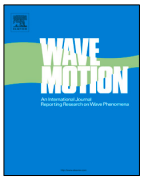

Variational Boussinesq model for kinematics calculation of surface gravity waves over bathymetry

Christopher Lawrence [a], Odin Gramstad [b], Karsten Trulsen [a,*]

[a] Department of Mathematics, University of Oslo, Norway
[b] DNV GL Group Technology and Research, Høvik, Norway

ARTICLE INFO

Article history:
Received 11 February 2020
Received in revised form 22 July 2020
Accepted 25 September 2020
Available online 17 October 2020

Keywords:
Variational Boussinesq model
Surface waves
Wave kinematics

ABSTRACT

Many of the widely used models for description of nonlinear surface gravity waves, in deep or shallow water, such as High Order Spectral Method (HOSM) and Boussinesq-type equations, rely on the elimination of the vertical coordinate from the basic three-dimensional Euler equations. From a numerical point of view such models are often computationally efficient, which is one of the main reasons that many such models are frequently used in studies on nonlinear surface waves.

While surface-based models provide the time-evolution of surface quantities, typically the surface elevation η and velocity potential at the surface ϕ, they do not directly provide the water particle kinematics in the fluid interior. However, in many practical applications information about the water-particle kinematics is crucial.

The present paper presents a new method for the calculation of water-particle kinematics, from information about surface quantities. The presented methodology is a non-perturbative approach based on the fully nonlinear Variational Boussinesq model, and can be applied to wave propagation over both constant and variable water depth. The proposed method is validated on several cases, including Stokes waves, a solitary wave, and irregular waves over flat bottom. We have carried out new laboratory experiments of regular waves over a shoal with measurements of the horizontal velocity specifically taken for validation of the method. We also employ recent laboratory experiments for validation of statistical properties of wave kinematics of long crested irregular waves propagating over a shoal.

1. Introduction

The accurate modeling of ocean surface waves is gaining attention from marine industry. In engineering applications, proper prediction of loads and responses of ships and offshore structures are essential. The wave loads acting on marine structures are related to the water particle kinematics generated by the waves, hence the accurate calculation of the kinematics is a crucial part of any wave model.

Conventionally, linear or second-order wave models are used by marine industry for ships or offshore structures design. However, neither linear nor second-order wave models can describe very high and steep waves realistically. There is therefore a need for more accurate wave models that are able to take higher-order nonlinear effects into account, and that are able to describe steep and nonlinear waves. In recent years, Computational Fluid Dynamics (CFD) computations have

* Correspondence to: Department of Mathematics, University of Oslo, PO Box 1053 Blindern, NO-0316 Oslo, Norway.
E-mail address: karstent@math.uio.no (K. Trulsen).

https://doi.org/10.1016/j.wavemoti.2020.102665

become increasingly used for wave-structure analysis. However, due to the computational cost of fully three-dimensional CFD simulations, computationally efficient approximate wave models are still needed in many applications. Note also that the computational domain, and consequently the computational cost of CFD simulations may be reduced by coupling CFD codes with computationally cheaper models like potential flow models. Naturally, efficient and accurate wave kinematics are needed for coupling to CFD codes.

The basic equations describing surface gravity waves on an ideal fluid are the Euler equations. Assuming potential theory (irrotational flow) the basic equations can be reformulated in Hamiltonian structure with the surface elevation η and velocity potential at the surface ϕ as canonical variables [1–4]. The elimination of the vertical dependence in the Euler equations has the potential to greatly improve the efficiency of time marching procedures in numerical solutions of the equations, due to the fact that a full discretization of the entire fluid domain can be replaced by a discretization of the horizontal plane only. In the long-wave (shallow water) regime the reduction of the problem to the horizontal plane leads to the Boussinesq and Korteweg–de Vries equations. In a modulational regime (deep and intermediate water depth) one has perturbative methods for solving the Euler equations, under assumption of deep or intermediate water depth, known as High Order Spectral Method (HOSM) [5,6] and equivalent methods [7,8], as well as more simplified models such as nonlinear Schrödinger-type equations [2,9].

While such surface-based methods are often numerically efficient, and provide surface quantities such as the surface elevation and velocity potential at the surface, they do not directly provide the water particle kinematics below the surface. Hence, additional computations are needed in order to provide water particle kinematics in an arbitrary point in the fluid domain. For linear waves in constant water depth an explicit solution of the Laplace boundary value problem is given by linear Airy theory. A method for calculation of kinematics based on the nonlinear Schrödinger equation was presented in [10], and was shown to give good agreement with laboratory measurements [11].

A fully nonlinear and direct solution for the wave kinematics, given a Fourier-representation of the wave field was suggested by [12]. This method involves solving a system of equations of the same dimensions as the number of Fourier components. Hence, in particular for short-crested sea states this method is typically too computationally expensive, and is also prone to numerical instabilities. Alternative methods based on iterative expansion of the Dirichlet to Neumann operators were presented in [13], often referred to as the H- and H_2-operator methods. Essentially these methods are natural extensions of the methodology employed in the original HOSM [5,6]. It was demonstrated in [13] that these methods could accurately calculate kinematics in short-crested waves relatively efficiently. However, the original HOSM with the H- and H_2-operator methods are only valid for flat bottom.

In this paper we present a method for calculation of the water particle kinematics that can also handle variable bathymetry. The proposed method is based on Variational Boussinesq model (VBM) [14,15], which is a non-perturbative method that solves the Laplace boundary value problem via Dirichlet's principle. Several works have been published on validation of VBM with respect to wave propagation [16–18]. In this paper we apply the VBM formulation for calculation of the water particle kinematics. Several validation tests are presented showing that the proposed method provides a robust and efficient way to calculate wave kinematics in a surface wave model.

The proposed methodology can be applied to any surface wave model that provides the surface elevation η and surface potential ϕ. In the present paper we have employed a HOSM with variable bottom topography for time evolution, as suggested in [19,20]. Compared to HOSM for constant depth [5], this method considers an additional velocity potential at the bottom and utilizes Taylor expansion to compute the modified surface vertical velocity with correct bottom boundary condition. The interior kinematics of HOSM for uneven bottom has not yet been derived. Therefore, VBM is applied to compute the interior kinematics after HOSM provides the information of the surface elevation η and surface potential ϕ. We emphasize that the accuracy of wave kinematics calculation still depends on the dynamic solution itself.

For validation, the VBM is compared to known solutions of Stokes waves and solitary waves. The H- and H_2-operator methods which are valid for flat bottom case are also employed for comparison. For uneven bottom, we conducted laboratory experiments of regular waves propagating over a shoal with surface elevation and horizontal velocity measurements to validate the VBM. The statistics of wave kinematics of irregular waves propagating over a shoal is also presented and compared with results from experimental data.

The organization of the paper is as follows. In Section 2, the Variational Boussinesq Model (VBM) is discussed in the context of kinematics calculation. For comparison, the H- and H_2- operator methods are also discussed briefly in Section 2. Validation of the proposed methodology, including comparison with existing methods and our experimental results are presented in Section 3. In Section 4 statistical properties of wave kinematics in random wave fields are investigated and compared to results from laboratory experiments. Finally, conclusions and discussion are given in Section 5.

2. Numerical method for kinematics calculation

We propose a numerical method for kinematics calculation based on Variational Boussinesq Model which will be discussed in Section 2.1. For comparison, we also describe briefly other numerical methods called the H- and H_2- operator methods in Section 2.2.

2.1. Variational Boussinesq model

We consider a three-dimensional inviscid and incompressible fluid bounded by an impermeable bottom $z = -h(\mathbf{x})$ and a free surface $z = \eta(\mathbf{x}, t)$, where $\mathbf{x} = (x, y)$ are the horizontal coordinates, z is the vertical coordinate and t is time. Let $\mathbf{U} = (u, v, w) = \mathbf{u} + w\mathbf{i}_z$ be the fluid velocity, where $\mathbf{u} = (u, v)$ are the horizontal velocities and w is the vertical velocity. By assuming irrotational flow, the fluid velocity can be written as $\mathbf{U} = \nabla\Phi$ where $\Phi(\mathbf{x}, z, t)$ denotes the velocity potential. For incompressible fluid, the continuity equation reduces to $\nabla \cdot \mathbf{U} = 0$. Consequently, the continuity equation becomes the Laplace equation in the fluid domain

$$\nabla \cdot \nabla\Phi = 0.$$

The kinematic and dynamic boundary conditions are given as

$$\begin{aligned} \mathbf{n_s} \cdot \nabla\Phi\sqrt{1 + |\nabla\eta|^2} &= \partial_t\eta, \quad \text{at} \quad z = \eta, \\ \partial_t\Phi + g\eta + \frac{1}{2}|\nabla\Phi|^2 &= 0, \quad \text{at} \quad z = \eta, \\ \mathbf{n_b} \cdot \nabla\Phi &= 0, \quad \text{at} \quad z = -h, \end{aligned} \tag{1}$$

where g is the acceleration of gravity, and

$$\mathbf{n}_s = \frac{-\nabla\eta + \mathbf{i}_z}{\sqrt{1 + |\nabla\eta|^2}} \quad \text{and} \quad \mathbf{n}_b = \frac{-\nabla h - \mathbf{i}_z}{\sqrt{1 + |\nabla h|^2}}$$

are the unit normal direction vectors at the surface and at the bottom pointing out of the fluid, respectively.

Defining the surface potential $\phi(\mathbf{x}, t) = \Phi(\mathbf{x}, z = \eta, t)$, it has been discovered by [2–4] that the dynamic Eqs. (1) have a Hamiltonian structure when expressed in the surface elevation η and surface potential ϕ. The Hamiltonian can be written as functional of the two canonical variables η and ϕ as a sum of the potential energy $\mathcal{P}(\eta)$ and kinetic energy $\mathcal{K}(\eta, \phi)$

$$\begin{aligned} \mathcal{H}(\eta, \phi) &= \mathcal{P}(\eta) + \mathcal{K}(\eta, \phi) \\ &= \frac{1}{2}\int g\eta^2 d\mathbf{x} + \frac{1}{2}\int\int_{-h}^{\eta} |\nabla\Phi|^2 \, dz d\mathbf{x}. \end{aligned} \tag{2}$$

where the following brief notation is used:

$$\int \bullet d\mathbf{x} = \iint \bullet dxdy$$

Consequently, the dynamics of the canonical variables η and ϕ are given by the Hamiltonian equations

$$\begin{aligned} \partial_t\eta &= \delta_\phi\mathcal{H}(\eta, \phi) \\ \partial_t\phi &= -\delta_\eta\mathcal{H}(\eta, \phi) \end{aligned} \tag{3}$$

where δ_ϕ and δ_η denote the variational derivatives with respect to ϕ and η respectively.

As introduced in [14], the velocity potential $\Phi(\mathbf{x}, z, t)$ can be approximated by adding z-dependent functions so that

$$\Phi_{VBM}(\mathbf{x}, z, t) = \phi(\mathbf{x}, t) + F_m(z; \eta, h)\psi_m(\mathbf{x}, t) \tag{4}$$

where m is a summation running from 1 to M according to Einstein notation and M is a small finite number of vertical profiles. F_m are vertical shape functions and ψ_m are amplitude functions. The condition at the surface $\Phi_{VBM}(\mathbf{x}, z = \eta, t) = \phi(\mathbf{x}, t)$ has to be fulfilled to keep the canonical structure of the Hamiltonian, and this can be achieved by requiring $F_m(z = \eta) = 0$ for all m. The bottom impermeability condition requires that the normal velocity at the bottom is zero.

The Variational Boussinesq Model (VBM) solves the Laplace equation $\nabla \cdot \nabla\Phi = 0$ via Dirichlet's principle. That is, the solution of the Laplace equation is found as the unique minimizer of the kinetic energy (see [21]). The vertical profiles F_m and the number of profiles M should be chosen in advance. Then the amplitude functions ψ_m are the subject of the kinetic energy minimization. The kinetic energy of VBM is given by

$$\begin{aligned} \mathcal{K}_{VBM}(\phi, \eta; \psi_m, \kappa_m) &= \frac{1}{2}\int\int_{-h}^{\eta} |\nabla\Phi_{VBM}|^2 \, dz d\mathbf{x} \\ &= \frac{1}{2}\int (h + \eta)(\nabla\phi)^2 + \alpha_{mn}\nabla\psi_m \cdot \nabla\psi_n + (\theta_{mn} + \gamma_{mn})\psi_m\psi_n \\ &\quad + 2\boldsymbol{\nu}_{mn}\psi_n \cdot \nabla\psi_m + 2\nabla\phi \cdot \left(\beta_m\nabla\psi_m + \boldsymbol{\xi}_m\psi_m\right) d\mathbf{x}, \end{aligned} \tag{5}$$

where the integrals over z are defined by

$$\begin{aligned} \alpha_{mn} &= \int_{-h}^{\eta} F_m F_n dz; \quad \beta_m = \int_{-h}^{\eta} F_m dz; \quad \gamma_{mn} = \int_{-h}^{\eta} \partial_z F_m \partial_z F_n dz; \\ \boldsymbol{\nu}_{mn} &= \int_{-h}^{\eta} F_m \nabla_H F_n dz; \quad \boldsymbol{\xi}_m = \int_{-h}^{\eta} \nabla_H F_m dz; \quad \theta_{mn} = \int_{-h}^{\eta} \nabla_H F_m \cdot \nabla_H F_n dz. \end{aligned} \tag{6}$$

Here, $(\nabla\phi)^2$ means the inner product $(\nabla\phi)\cdot(\nabla\phi)$ and ∇_H is horizontal gradient.

Various types of vertical profiles function were discussed in [15]. In this paper, we choose the normalized hyperbolic cosine functions which is called Airy profile in [17,18]

$$F_m(z;\eta,h) = \frac{\cosh\left[\kappa_m(z+h)\right]}{\cosh\left[\kappa_m(\eta+h)\right]} - 1. \tag{7}$$

Note that κ_m are not the actual wavenumbers but are just parameters that can be optimally chosen depending on the case. For flat bottom, κ_m are constants. In general, the water depth h is a function of $\mathbf{x}$. Inspired by Ray theory for slowly varying bottom, we use a local linear dispersion relation $\underline{\omega}_m = \sqrt{g\kappa_m \tanh \kappa_m h(\mathbf{x})}$ where $\underline{\omega}_m$ are constant along the bathymetry. Since $\underline{\omega}_m$ are constant and h is a function of $\mathbf{x}$ then κ_m are functions of $\mathbf{x}$ for uneven bottom. In most cases, and in the cases we consider, two or three Airy profiles are sufficient to obtain good dispersion properties over the range of wavenumber of wave frequencies of interest. The optimal choice of κ_m will be described in detail in Section 2.1.1.

In [17], the variations of vertical profiles F with respect to $\mathbf{x}$ were neglected, i.e.

$$\partial_\eta F_m \nabla\eta,\ \partial_h F_m \nabla h,\ \partial_\kappa F_m \nabla\kappa \approx 0. \tag{8}$$

They called this simplification *weakly nonlinear* VBM and showed that it gives good agreement with laboratory experiments in bichromatic waves and irregular waves propagating over a 1:20 slope. As an improvement, [18] includes the effects of $\partial_\eta F_m \nabla\eta$, but the effects of the bed slope ∇h and parameter variations $\nabla\kappa$ were neglected. It turned out that *weakly nonlinear* VBM gives unsatisfactory results for strongly nonlinear waves, e.g. a focusing wave group. For steep slopes, this approximation does not perform well with respect to reflection and may introduce high frequency waves. However, taking all the terms into consideration ('steep slope' models in [22]) gives good reflection characteristics up to bottom slope 2:5, despite the usage of vertical shape functions with $\partial_z F = 0$ at the bottom and the approximation based on slowly varying bottom.

In this paper, the VBM is not used for wave propagation but only to compute the velocity potential in the fluid. Here, the contribution from ∇F_m is fully taken into account. The difference with the previous approach [18] will be shown in Section 3.4. The amplitude functions ψ_m are then obtained by minimizing kinetic energy, by requiring that $\delta_{\psi_n} K = 0$, leading to a system of linear elliptic equations

$$-\nabla\cdot(\alpha_{mn}\nabla\psi_n) + (\theta_{mn}+\gamma_{mn})\,\psi_n + \boldsymbol{\nu}_{nm}\cdot\nabla\psi_n - \nabla\cdot(\boldsymbol{\nu}_{mn}\psi_n) = \nabla\cdot(\beta_m\nabla\phi) - \boldsymbol{\xi}_m\cdot\nabla\phi. \tag{9}$$

When ψ_m are found from (9), the kinematics at any z can be easily obtained from (4).

The VBM approximation in (4) will give its own linear dispersion relation, which is described in the following.

One can show that the kinetic energy of linear VBM is obtained by taking $\eta = 0$ in (5)

$$\mathcal{K}_{VBM}^{(lin)} = \frac{1}{2}\int \left[h\,(\nabla\phi)^2 + \bar{\alpha}_{mn}\nabla\psi_m\cdot\nabla\psi_n + \bar{\gamma}_{mn}\psi_m\psi_n + 2\bar{\beta}_m\nabla\phi\cdot\nabla\psi_m\right] d\mathbf{x}, \tag{10}$$

where the coefficients $\bar{\alpha}_{mn}$, $\bar{\beta}_{mn}$ and $\bar{\gamma}_{mn}$ are given by (6), but with the integration performed from $z=-h$ to still water level $z=0$.

The linear dynamic equations of VBM are obtained by taking variations of $\mathcal{H}_{VBM}^{(lin)} = \mathcal{P} + \mathcal{K}_{VBM}^{(lin)}$ with respect to η, ϕ and ψ_n. The linear VBM is given as

$$\begin{aligned} &\partial_t\eta = -h\nabla\cdot\nabla\phi - \bar{\beta}_m\nabla\cdot\nabla\psi_m \\ &\partial_t\phi = -g\eta \\ &-\bar{\alpha}_{mn}\nabla\cdot\nabla\psi_n + \bar{\gamma}_{mn}\psi_n = \bar{\beta}_m\nabla\cdot\nabla\phi. \end{aligned} \tag{11}$$

We find the dispersion relation of VBM by considering simple harmonic waves with frequency $\omega = \Omega_{VBM}(k)$ which depends on the wave number $k = |\mathbf{k}|$:

$$\eta = \hat{\eta}e^{i(\mathbf{k}\cdot\mathbf{x}-\omega t)}, \quad \phi = \hat{\phi}e^{i(\mathbf{k}\cdot\mathbf{x}-\omega t)}, \quad \psi_m = \hat{\psi}_m e^{i(\mathbf{k}\cdot\mathbf{x}-\omega t)}. \tag{12}$$

Substituting (12) into the linear system of VBM (11) will give matrix equation $M(\hat{\eta},\hat{\phi},\hat{\psi}_m)^T = 0$, where non-trivial solutions exist when $\det M = 0$. The resulting dispersion relation strongly depends on the parameters κ_m in (7), and is given by

$$C_{VBM}^2 = \left(\frac{\Omega_{VBM}(k)}{k}\right)^2 = c_0^2\left(1 - \frac{k^2}{h}\bar{\beta}_m(\bar{\alpha}_{mn}k^2 + \bar{\gamma}_{mn})^{-1}\bar{\beta}_n\right) \tag{13}$$

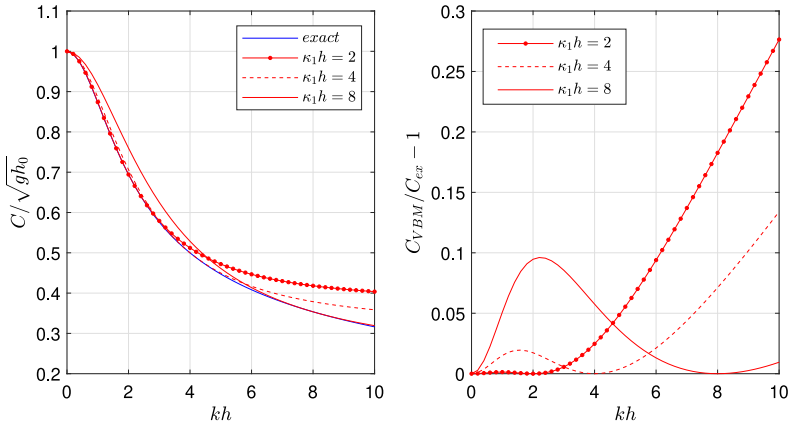

Fig. 1. Linear dispersion characteristics of VBM one-profile. Left: Comparison of normalized phase speed of VBM with one profile with $\kappa_1 h = 2, 4, 8$ to exact solution. Right: Relative error in the phase speed of VBM with one profile.

where C_{VBM} is the phase speed of VBM, and $c_0 = \sqrt{gh}$. For multiple profiles F_m, given by (7), we require the parameters κ_m to have different values so that the matrix $(\bar{\alpha}_{mn}k^2 + \bar{\gamma}_{mn})$ is invertible. The exact phase speed is given as

$$C_{ex}^2 = \left(\frac{\Omega_{ex}(k)}{k}\right)^2 = \frac{g\tanh(kh)}{k}. \tag{14}$$

As pointed out in [16], the approximate phase speed of VBM, C_{VBM}, is larger than or equal to the exact phase speed, C_{ex}. This is an implication from minimization of kinetic energy. For VBM with Airy profile in (7), VBM has exact phase speed only for the wavenumbers $k = \kappa_m$.

$$C_{VBM}(k) > C_{ex}(k) \quad \text{for } k \neq 0, \kappa_m \quad \text{and} \quad C_{VBM}(\kappa_m) = C_{ex}(\kappa_m) \quad \text{for all } m. \tag{15}$$

For example, linear dispersion characteristics of VBM with one profile with different parameters κ are shown in Fig. 1.

2.1.1. Dispersion optimization

The flexibility to choose the number of vertical profiles M and the parameters κ_m means that VBM dispersion can be optimized to approximate the exact linear dispersion depending on the problem. There are several optimization criteria to choose parameters κ_m, e.g. minimize phase speed or group speed error over the range of the relevant wavenumbers or wave frequencies, but the optimization criteria based on kinetic energy performs better than the others [23]. In [16], these parameters were chosen by minimizing the kinetic energy based on the initial spectrum. However, in a nonlinear simulation the initial spectrum will be deformed during the time evolution, especially in the tail of the spectrum when strong nonlinear effects are present. Therefore, the optimization of the parameters κ_m should be based on the deformed spectrum as in [18]. The optimization of the parameters κ_m based on kinetic energy minimization is discussed in the following.

Let the Fourier transform pair be defined as

$$f(x) = \int \hat{f}(k)e^{ikx}dk \quad \text{and} \quad \hat{f}(k) = \frac{1}{2\pi}\int f(x)e^{-ikx}dx. \tag{16}$$

The kinetic energy of the linear VBM can then be written as

$$\mathcal{K}_{VBM}^{(lin)}(\phi;\kappa) = \frac{2\pi}{2g}\int \Omega_{VBM}^2(k;\kappa)\left|\hat{\phi}(k)\right|^2 dk. \tag{17}$$

By using Dirichlet's principle, the optimal choice of parameters κ_m would be the minimizer of

$$\underset{\kappa_1,\ldots,\kappa_M}{\arg\min}\int \Omega_{VBM}^2(k;\kappa_1,\ldots,\kappa_M)\left|\hat{\phi}(k)\right|^2 dk. \tag{18}$$

Note that we here consider the kinematic calculation as post-processing, i.e. that $\eta(x,t)$ and $\phi(x,t)$ are known. For flat bottom, the weight function $|\hat{\phi}(k)|^2$ can be calculated for any time t. To give the best possible dispersion properties over the desired k-range, we choose the broadest spectrum during the chosen time evolution as the weight function. For uneven bottom, wavenumber-parameters κ_m are functions of x, but the corresponding parameters $\underline{\omega}_m = \sqrt{g\kappa_m\tanh(\kappa_m h)}$ are constant along the bathymetry which is inspired by Ray theory. Fig. 2 illustrates the relation between Ω_{VBM}, Ω_{ex} and

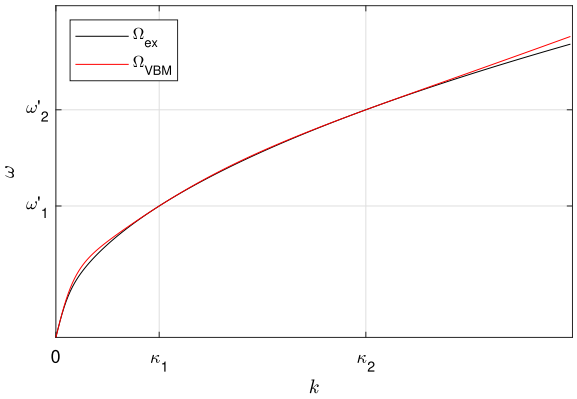

Fig. 2. Illustration for linear dispersion relation of VBM with two profiles.

parameters κ_m and $\underline{\omega}_m$. We can modify the arguments of the minimization problem in (18) to the parameters $\underline{\omega}_m$. In order to do this, we have to express the kinetic energy in terms of time series $s(t) = \eta(x = x_0, t)$ where it has the broadest spectrum in the entire domain. For linear unidirectional waves, the procedure will be given as follows.

The exact linear dispersion relation is given as $\Omega_{ex}(k) = \sqrt{gk\tanh(kh)}$. Defining $\Omega_{ex}^{-1}(\omega) = k$ as the inverse function of $\Omega_{ex}(k) = \omega$, and letting $\tilde{s}(\omega)$ denote the temporal Fourier transform of $s(t)$, it holds that

$$\eta(x_0, t) = \int \tilde{s}(\omega) e^{i(\Omega_{ex}^{-1}(\omega)x_0 - \omega t)} d\omega = \int \hat{s}(\Omega_{ex}(k)) e^{i(kx_0 - \Omega_{ex}(k)t)} V(k) dk \tag{19}$$

where $V(k) = \partial_k \Omega_{ex}(k)$ is the group speed of the exact linear dispersion relation.

Further, taking the Fourier-transform of the linear momentum equation $\partial_t \phi = -g\eta$ yields $i\Omega_{ex}(k)\hat{\phi}(k, t) = g\hat{\eta}(k, t)$. Since $\eta(x, t) = \int \hat{\eta}(k, t) e^{ikx} dk$ it follows that $\hat{\eta}(k, t) = \hat{s}(\Omega_{ex}(k)) e^{-i\Omega_{ex}(k)t} V(k)$, so that

$$|\hat{\phi}(k, t)|^2 = \left(\frac{g\hat{s}(\Omega_{ex}(k))V(k)}{\Omega_{ex}(k)} \right)^2. \tag{20}$$

Now the kinetic energy (17) can be rewritten as

$$\begin{aligned} \mathcal{K}_{VBM}^{(lin)}(\phi; \underline{\omega}) &= \pi g \int \left|\hat{s}(\Omega_{ex}(k))\right|^2 \left(\frac{\Omega_{VBM}(k; \kappa)}{\Omega_{ex}(k)} \right)^2 V(k)^2 dk \\ &= \pi g \int \left|\tilde{s}(\omega)\right|^2 \left(\frac{\Omega_{VBM}(\Omega_{ex}^{-1}(\omega); \underline{\omega})}{\omega} \right)^2 V(\Omega_{ex}^{-1}(\omega)) d\omega \end{aligned} \tag{21}$$

and the minimization problem in (18) becomes

$$\underset{\underline{\omega}_1, \ldots, \underline{\omega}_M}{\arg\min} \int \left(\frac{\Omega_{VBM}(\Omega_{ex}^{-1}(\omega); \underline{\omega}_2, \ldots, \underline{\omega}_M)}{\omega} \right)^2 V(\Omega_{ex}^{-1}(\omega)) \left|\tilde{s}(\omega)\right|^2 d\omega. \tag{22}$$

Here we choose the broadest spectrum $\left|\tilde{s}(\omega)\right|^2$ to be solved in (22).

2.2. H- and H_2- operator

Two wave kinematics calculation methods based on information from surface variables were presented in Dirichlet to Neumann formulation by [13]. The first method is the so-called H- operator which transforms any information at the surface to constant z-level. However, it has been shown that the H- operator can be divergent beneath large wave crests since the accuracy itself is related to the convergence of Taylor series. As a remedy, the so-called H_2- operator performs the transformation to a second arbitrary surface therefore it allows the transformation from the surface to constant z-level in several small steps. We give brief review of these two operators in the following.

Let $\tau(x, z, t)$ denote an arbitrary kinematic quantity. We assume $\tau(x, z, t)$ can be represented as

$$\tau(x, z, t) = \int \hat{\tau}(k) \frac{\cosh(k(z + h))}{\cosh(kh)} e^{i(kx - \omega t)} dk \tag{23}$$

where $\omega(k) = \sqrt{gk\tanh(kh)}$ is wave frequency, k is wavenumber, g is acceleration of gravity, and h is water depth. Eq. (23) is suitable for kinematics quantities whose the vertical variation is described by the summation of cosh terms such as

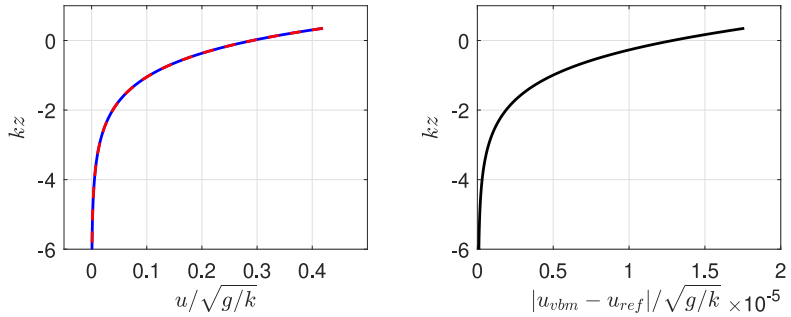

Fig. 3. Left: vertical profile of horizontal velocity of Stokes wave with $ka = 0.3$ and $kh = 10$ (VBM: red dashed line, reference solution: blue solid line). Right: absolute error of the corresponding horizontal velocity presented in the left plot.

surface potential ϕ or horizontal velocity $u = \partial\Phi/\partial x$. For an alternative conjugate variable such as vertical velocity $w = \partial\Phi/\partial z$, the numerator in Eq. (23) should be replaced by sinh.

For H- operator, the kinematic quantity τ is transformed to $z = 0$ by using Taylor series and perturbation approach similar to HOSM [5,6]

$$\begin{aligned} \tau^{(1)}(x,0,t) &= \tau(x,\eta,t) \\ \tau^{(m)}(x,0,t) &= -\sum_{n=1}^{m-1} \frac{\eta^n}{n!} \frac{\partial^n \tau^{(m-n)}}{\partial z^n}(x,0,t), \quad m \geq 2, \end{aligned} \tag{24}$$

where the superscript on τ indicate the nonlinearity order of τ. For instance $\tau^{(1)} \equiv O(\epsilon)$ where ϵ is the wave steepness.

For H_2- operator, the kinematic quantity τ is transformed to a second arbitrary surface $z = c\eta_2$ with $c < 1$. Subsequently, the transformation is repeated to a new smaller arbitrary surface $z = \eta_{2,new} = c\eta_{2,old}$ with $c < 1$. This process is repeated until constant z-level. The difference with the H- operator is the transformation in H_2- operator is done with several small steps, meanwhile the H- operator transform only in a single step. Typically, H_2- operator converges with only ten number of steps. Note that H_2- operator is equivalent to H- operator when the new arbitrary surface is zero $\eta_2 = 0$. The kinematic quantity τ at $z = \eta_2$ is given by Taylor expansion as

$$\tau^{(m)}(x, z = \eta_2, t) = \sum_{n=0}^{m-1} \frac{\eta_2^n}{n!} \frac{\partial^n \xi^{(m-n)}}{\partial z^n}(x,0,t). \tag{25}$$

3. Validation

In order to test and validate the proposed methodology for kinematics calculation, several validation tests are presented in the four subsections below. First we consider Stokes wave in deep water, comparing results with Fenton's fifth order solution [24]. In Section 3.2 we consider a solitary wave in constant depth, comparing the results with the high-accuracy solution of the exact Euler equations given in [25], as well as results using the H_2-operator method [13]. In Section 3.3 the case of irregular waves over flat bottom is presented and compared to results using the H_2-operator method. Three different non-dimensional depths are considered, and the influence of the number of parameters and optimization-procedure in VBM is demonstrated. Finally, in Section 3.4, the case of regular waves over a shoal is considered and results are compared with new laboratory experiments.

3.1. Stokes wave

We consider Stokes waves in deep water with $ka = 0.3$ and $kh = 10$, where a is the first-order amplitude, k is the wavenumber and h is the water depth. The surface elevation $\eta(x,t)$ and surface potential $\phi(x,t)$ are obtained from Fenton's fifth order solution [24]. The surface potential is found by evaluating the fifth order velocity potential as $z = \eta$, retaining fifth order terms. Then the VBM proposed above was used to calculate the corresponding wave kinematics. In this case, we use VBM with three profiles. Fig. 3 shows the horizontal velocity profile under the wave crest, compared with Fenton's solution. Fig. 4 shows the normalized horizontal velocity at $kz = -0.5$ as function of x. As seen from the figures, the VBM reproduces the reference solutions to high accuracy.

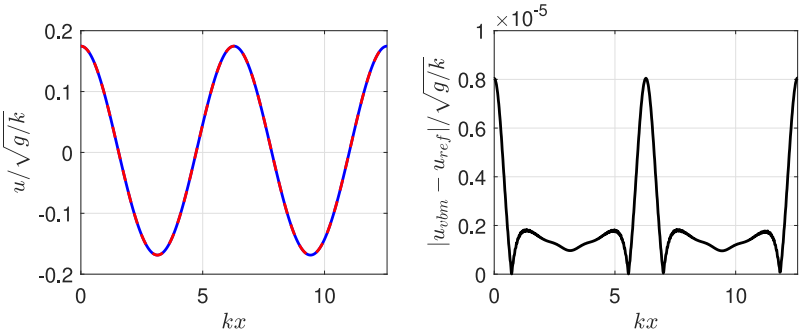

Fig. 4. Left: horizontal velocity of Stokes wave with $ka = 0.3$ and $kh = 10$ at $kz = -0.5$ (VBM: red dashed line, reference solution: blue solid line). Right: absolute error of the corresponding horizontal velocity presented in the left plot.

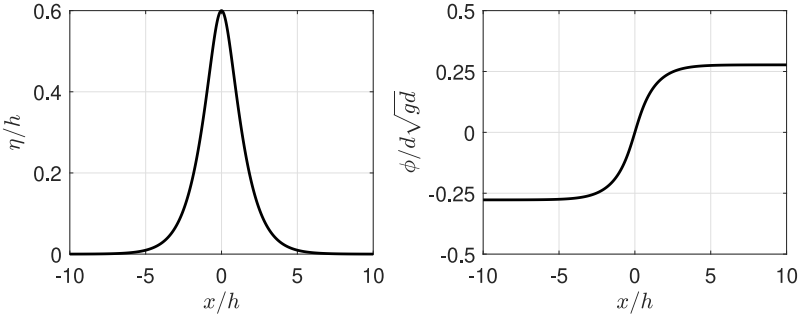

Fig. 5. The initial wave elevation (left plot) and velocity potential at surface. (right plot) with $a/h = 0.6$.

Table 1
Root mean square error (RMSE) of horizontal velocity of solitary wave at $z/h = -0.1$ for $x/h \in [-10, 10]$ relative to reference solution.

Method	Number of steps				
	5	10	15	20	30
5th order H_2	$5.0 \cdot 10^{-2}$	$7.6 \cdot 10^{-3}$	$6.0 \cdot 10^{-3}$	$5.3 \cdot 10^{-3}$	$4.7 \cdot 10^{-3}$
7th order H_2	$1.1 \cdot 10^{-2}$	$9.0 \cdot 10^{-4}$	$6.8 \cdot 10^{-4}$	$6.0 \cdot 10^{-4}$	$5.3 \cdot 10^{-4}$
9th order H_2	$5.9 \cdot 10^{-4}$	$2.2 \cdot 10^{-4}$	$1.8 \cdot 10^{-4}$	$1.6 \cdot 10^{-4}$	$1.4 \cdot 10^{-4}$
VBM			$1.1 \cdot 10^{-4}$		

3.2. Solitary wave

We consider the case of a nonlinear solitary wave in shallow water, with $a/h = 0.6$, where a is the amplitude and h is the water depth. In [25], the solitary wave solution of the exact Euler equations was computed numerically, including the wave kinematics in the bulk of the fluid. We used their code to compute the solitary wave solution as our reference. Using the information of surface elevation and surface potential from the reference solution, we used the VBM with three profiles to calculate the kinematics, and compared the results to both the reference solution as well as to the corresponding results obtained using the H_2-operator method proposed in [13]. The surface elevation and surface potential of the solitary wave are shown in Fig. 5, while Figs. 6 and 7 show the corresponding horizontal velocity for VBM compared to both the exact solution of [25] and the results obtained with 5th order H_2 operator with ten steps at $z/h = -0.1$ and $x = 0$, respectively. In addition, Fig. 8 shows the Laplacian of VBM velocity potential for three different number of profiles.

Table 1 shows the root-mean-square error (RMSE) of the horizontal velocity at $z/h = -0.1$ for $x/h \in [-10, 10]$ relative to the reference solution, for VBM and for the H_2-operator method using different nonlinear order and number of steps (see [13] for details).

As seen from the table, the VBM reproduces the kinematics to high accuracy. Results are also in agreement with the H_2-operator method, but a quite high order and a large number of steps are needed for the H_2-operator to give the same accuracy as the VBM.

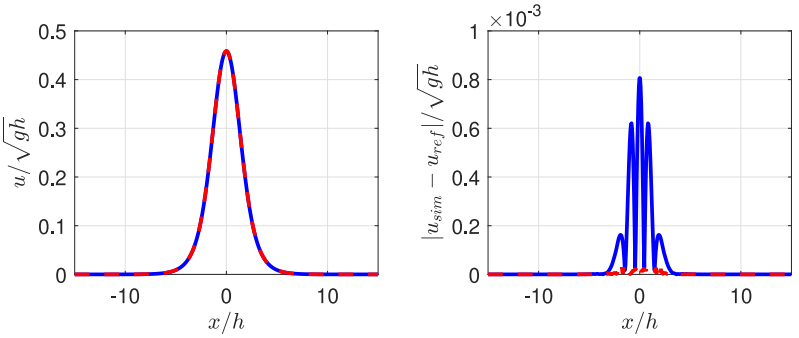

Fig. 6. Left: horizontal velocity of solitary wave at offset $z/h = -0.1$. Right: absolute error of the simulated horizontal velocity with reference solution in [25]. (VBM: red dashed line. H_2 operator: blue solid line).

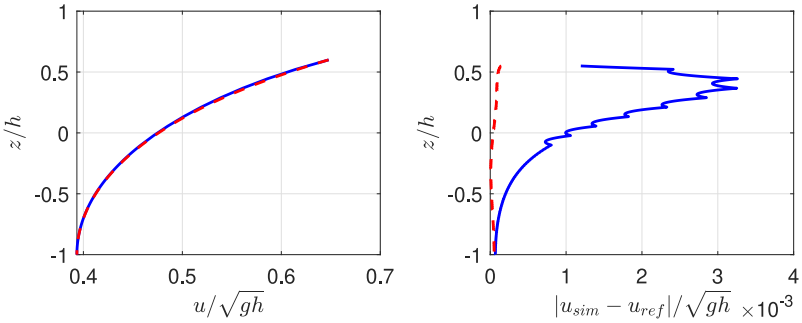

Fig. 7. Left: vertical profile of horizontal velocity of solitary wave. Right: absolute error of the simulated horizontal velocity with reference solution in [25]. (VBM: red dashed line. H_2 operator: blue solid line).

Table 2
Nondimensional optimal parameters $\underline{\omega}_m/\omega_p$ of VBM and root mean square error compared to H_2-operator results.

Case	k_ph	VBM one profile		VBM two profiles		VBM three profiles	
		RMSE	$\underline{\omega}_m/\omega_p$	RMSE	$\underline{\omega}_m/\omega_p$	RMSE	$\underline{\omega}_m/\omega_p$
1	1	0.0140	1.58	0.0008	1.31, 3.04	0.0006	1.21, 2.39, 4.00
2	3	0.0291	1.28	0.0060	1.06, 2.18	0.0010	1.00, 1.65, 3.09
3	10	0.0338	1.2	0.0099	1.00,1.97	0.0013	0.94, 1.40, 2.71

3.3. Irregular waves over flat bottom

In the following we consider irregular waves defined by a JONSWAP spectrum with peak enhancement factor $\gamma = 3.3$, peak wavenumber $k_p = 1$ m^{-1} and significant wave height $H_s = 0.16$ m. Three different water depths are considered: $h = 1$ m, 3 m and 10 m, for cases 1, 2 and 3, respectively.

For simulating the evolution of the irregular wave fields we use the High Order Spectral Method (HOSM), as described by [5]. For calculation of the water particle kinematics we use the VBM with one, two and three profile(s) as well as the H_2-operator method. Following recommendations given in [13], we have used 5th order H_2-operator with ten steps. In the following we present comparison of the horizontal velocity u at $k_pz = -0.2$.

As discussed in Section 2.1.1, for flat bottom the parameter-optimization may be done in terms of κ_m directly, using (18). However, as also discussed in Section 2.1.1, it is also possible do the optimization with respect to $\underline{\omega}_m$. Here, we use the latter option since it is more general and can be applied also for the uneven bottom case.

Figs. 9–11 show the corresponding linear dispersion fits of VBM, in terms of the relative error in phase-speed (left plot) and the calculated horizontal velocity at nondimensional depth $k_pz = -0.2$ (right plot). Table 2 summarizes the optimal values for $\underline{\omega}_m$ as well as the RMSE of VBM relative to the corresponding solution using the H_2-operator method.

For VBM with Airy profile, the dispersion relation is exact for $\omega = \underline{\omega}_m$ (see [16]). Without any optimization procedure, we expect the parameters $\underline{\omega}_m$ to be close to the peak frequency of the broad band waves. Nevertheless, for VBM with

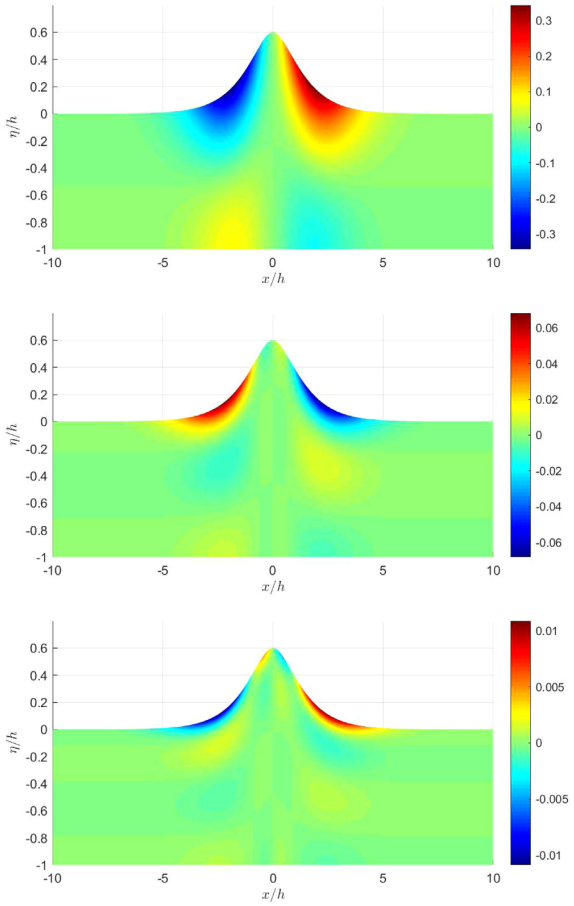

Fig. 8. Laplacian of VBM velocity potential for one profile (top), two profiles (middle) and three profiles (bottom).

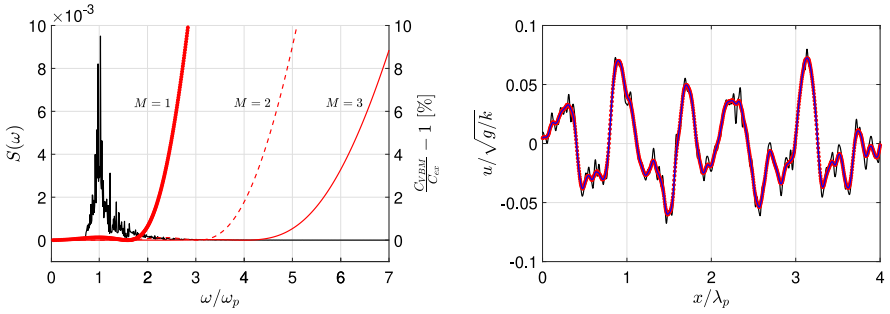

Fig. 9. Irregular waves over flat bottom case 1, Left: the wave spectrum (black solid line, left axis) is plotted together with the phase speed error for VBM with one, two and three profile(s) (red line with dots, dashed line, solid line, respectively). Right: Comparison between VBM with one profile (black, solid), VBM with three profiles (red with dots) and H_2 operator (blue, solid). (For interpretation of the references to color in this figure legend, the reader is referred to the web version of this article.)

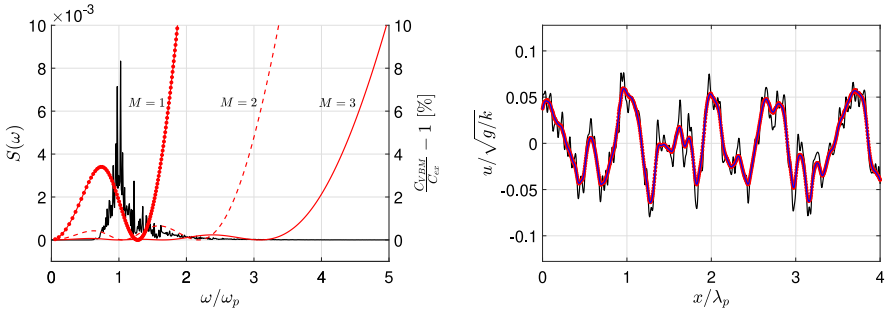

Fig. 10. Same as Fig. 9 for case 2.

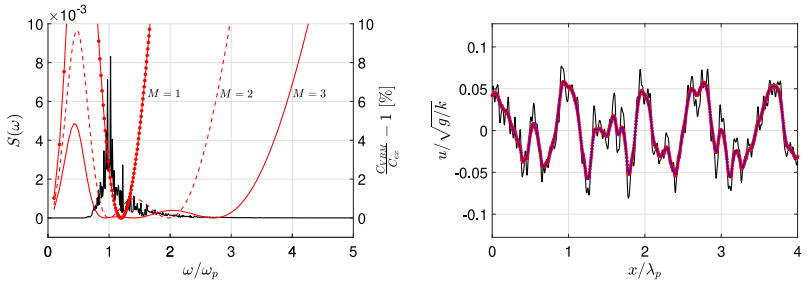

Fig. 11. Same as Fig. 9 for case 3.

one profile the optimal choice of parameter is not the peak frequency as shown in Table 2. For multiple profiles VBM, the optimal parameters are distributed so that the VBM dispersion fits the exact dispersion relation for the relevant wave spectrum as shown in Figs. 9, 10, 11.

It is observed that VBM gives good agreement with the H_2-operator result. As seen in Fig. 9, VBM with two profiles has excellent dispersion for the case with $k_p h = 1$. Hence, for shallow water depth, we are confident that two profiles are sufficient to calculate the kinematics accurately. Larger $k_p h$, however, requires a larger number of profiles. However, our results show that even for $k_p h = 10$, three profiles give excellent results.

3.4. Regular waves over a shoal

Several experimental studies of harmonic wave propagation over a shoal with different configurations are reported in the literature (e.g. [26–28]). However, in all of these studies only the surface elevation was measured and reported. For the present application of validating the VBM for calculation of kinematics, we also need the interior wave kinematics as the waves propagate over the shoal.

Wave tank experiments were therefore carried out in the 24.6 m long and 0.5 m wide wave tank at the Hydrodynamical Laboratory of Department of Mathematics at the University of Oslo. A shoal consisting of linear upslope and downslope regions of lengths 1.6 m separated by a 1.6 m flat region, reaching 0.42 m over the bottom of the tank. The still water depth away from the submerged bar was 0.53 m, corresponding to a water depth of 0.11 m at the top of the bar. At one end of the tank there is a wavemaker, and at the other end there is a wave absorber. The distance from the wavemaker to the center of the bar was 12.4 m. The shoal employed in these experiments was the same as that employed in [29].

Surface elevation measurements were made with four ultrasound probes from General Acoustics, while water velocity measurements were made with a "Vectrino" Acoustic Doppler Velocimeter (ADV) from Nortek. An overview of the experimental setup, with the installed measurement devices is shown in Fig. 12. The horizontal velocities were measured at depth 0.05 m below the still water level.

The wavemaker generated harmonic waves with frequency 0.7 Hz, and the wave amplitude was tuned as high as possible in order to have as nonlinear waves as possible, but without visible wave breaking. The experiments were repeated 31 times, having the measurement rig at different locations. For each run, the surface elevation was recorded at four locations, while the horizontal velocity was recorded at one location. Hence, in total the 31 runs provided the surface elevation at 124 locations and the horizontal velocity at 31 locations. In all cases, the measurements were completed before reflected waves arrived at the measurement-locations.

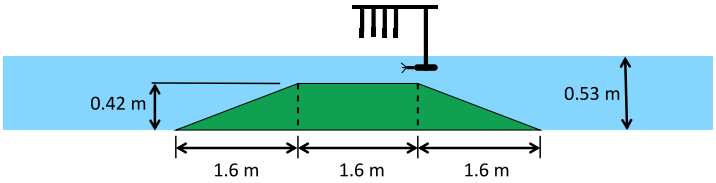

Fig. 12. Lay out of experimental setup with installed wave probes and ADV on top of the shoal.

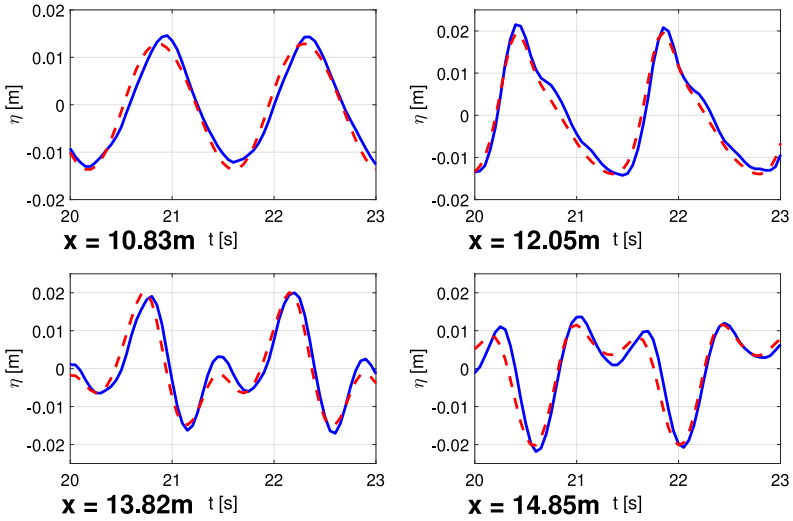

Fig. 13. Time series of surface elevation. Blue line: measurements. Red dashed line: HOSM simulation.

For validation of the kinematics calculations, numerical simulations corresponding to the experiments were carried out using a High Order Spectral Method (HOSM) that was modified to allow for variable depth, as described by [19,20]. The nonlinear order of the modified HOSM was set to third order on the surface and ninth order on the bottom (see [19,20] for details). The harmonic waves with frequency 0.7 Hz and amplitude 1.35 cm were generated 5.5 m before the shoal in numerical simulations using the embedded influxing method described in [30]. The wave amplitude was chosen so that the surface elevation fits the experimental data in front of the shoal.

Examples of surface elevation time series from the experiments and the numerical simulations, at four different locations, are shown in Fig. 13. Further, harmonic analysis of the surface elevation at different locations over the shoal is shown in Fig. 14. As expected, higher harmonic bound waves are strongly amplified when waves propagate over the shoal. Overall there is a good agreement between the experiments and the numerical simulations. However, some deviations between the experimental and numerical results are observed, in particular at the top of the bar and in the downslope region. This can likely be attributed to effects of bottom friction and dissipation from the sidewalls.

In this particular case, we show the difference of present VBM solution with previous method in [18]. It is shown in Fig. 15 that the missing contribution of ∇F in the kinetic energy to calculate amplitude function ψ may lead to instabilities around depth transition. It is also mentioned in [18] that for steep bottom slope, short waves were introduced in their dynamic evolution and some filtering was necessary.

For validation of the kinematics calculations, we use the horizontal velocity at depth 0.05 m provided by the experiments. The experimental results are then compared to the kinematics obtained by the VBM, which uses information about the surface elevation η and surface potential ϕ at every time step of the HOSM simulations. Time series of the horizontal velocity at four selected locations along the shoal are shown in Fig. 16. The corresponding evolution of the amplitudes of the different harmonic components of the velocity is shown in Fig. 17.

It is observed that the numerical results overestimate the first harmonic of the horizontal velocity after the upslope region. This may partly be explained by the fact that the measurement device interferes with the fluid flow. This has also been observed in tests with Stokes waves, in which case ADV measurements were found to underestimate the horizontal velocity compared to the analytical solution. However, for the second harmonic there is a good agreement, and overall the VBM-results show good agreement with the experimental results.

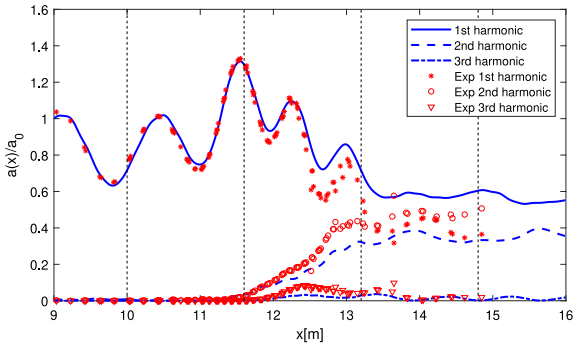

Fig. 14. Harmonic analysis of surface elevation.

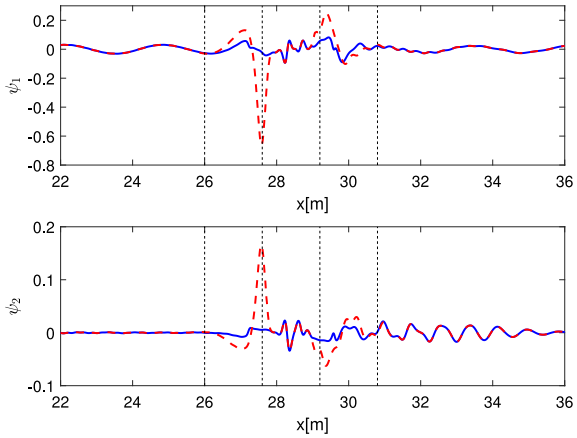

Fig. 15. Snapshot of amplitude functions ψ at $t = 20.8$ s with contribution from $\nabla_H F$(blue, solid) and without contribution from $\nabla_H F$(red, dashed).

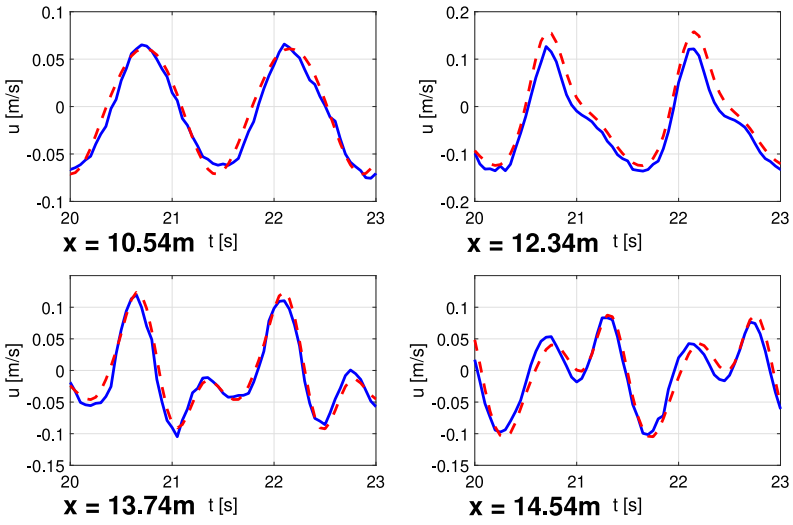

Fig. 16. Time series of horizontal velocity at depth 0.05 m. Blue line: measurements. Red dashed line: VBM simulation.

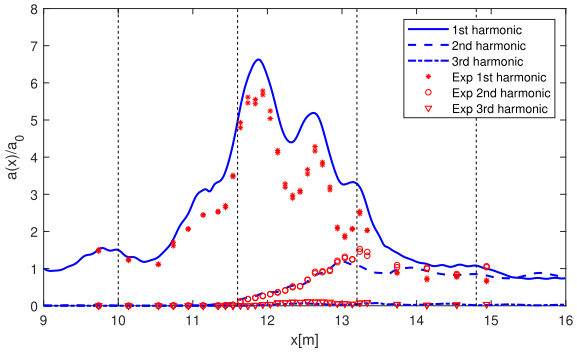

Fig. 17. Harmonic analysis of horizontal velocity at depth 0.05 m.

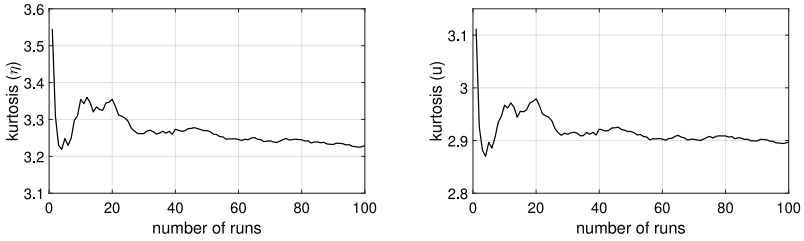

Fig. 18. Convergence of ensemble-averaged kurtosis at center of shoal with respect to number of runs in the ensemble. Left: kurtosis for surface elevation. Right: kurtosis for interior horizontal velocity at depth 0.04 m.

4. Statistical properties of irregular waves over a shoal

In this section we present an application of the VBM for kinematics calculations by investigating statistical properties of wave kinematics in irregular wave fields propagating over a shoal as in Fig. 12, and comparing the results to recent laboratory experiments [29].

It was reported in [29] that while the kurtosis of both surface elevation and interior fluid velocity experience an increase when propagating over the shoal, the locations of maximum kurtosis were different for surface elevation and wave kinematics. The laboratory setup for run 3 in [29] is similar to the one described in Section 3.4. However, in this case the wavemaker generated an irregular wave field having a JONSWAP spectrum with peak enhancement factor $\gamma = 3.3$ and peak period $T_p = 1.1$ s. The significant wave height was tuned as high as possible without observing visible wave breaking. The computed significant wave height before the slope was measured to $H_s = 2.5$ cm.

In the following we present numerical simulations corresponding to the experiments described in [29]. For the wave evolution the HOSM-model modified to allow for variable water depth [19,20], as described above, was used, while the VBM was used for the calculation of kinematics. As in the experiments the incoming waves were generated from a JONSWAP spectrum with peak enhancement factor $\gamma = 3.3$, peak period $T_p = 1.1$ s and significant wave height $H_s = 2.5$ cm. The numerical simulations were repeated 100 times, using different phases of the incoming wave train each run. For each run, time series of duration $200T_p$ were obtained. From these time series, the kurtosis and skewness of both surface elevation and horizontal velocity u at three different depths $z = -0.04$ m, $z = -0.06$ m and $z = -0.08$ m were computed by averaging over the time-series, and ensemble averaging over the 100 random repetitions. The convergence of the estimated kurtosis at the center of the shoal, as a function of the number of random repetitions is shown in Fig. 18. This indicates that 100 runs are sufficient to obtain relatively reliable estimates of the statistical quantities.

In Fig. 19, we show statistics of the surface elevation and the interior horizontal velocity at three different depths, from the numerical simulation. The skewness of the surface elevation and the horizontal velocities at all three depths show a similar evolution when propagating over the shoal. However, the magnitude of the skewness is decreasing with increasing depth.

Different from the skewness, the evolution of kurtosis of the surface elevation and the horizontal velocities show qualitatively different behavior when propagating over the shoal. The kurtosis of the horizontal velocity has a local maximum on the lee side and a local minimum on top of the shoal, while the kurtosis of the surface elevation has its local maximum at the top of the shoal. These results are in good agreement with the results of the laboratory experiment in [29], as shown in Fig. 20.

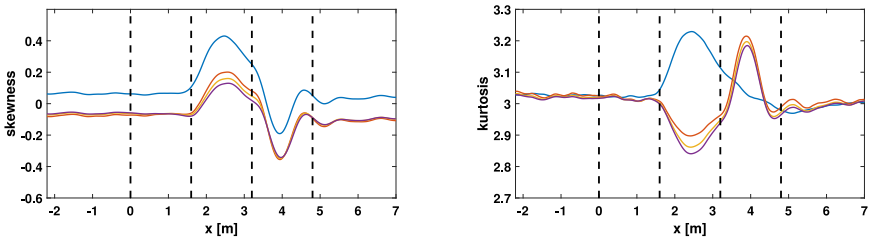

Fig. 19. Skewness (left) and kurtosis (right) of surface elevation (blue) and horizontal velocity at depth 0.04 m (red), 0.06 m (yellow), and 0.08 m (purple) from numerical simulation. (For interpretation of the references to color in this figure legend, the reader is referred to the web version of this article.)

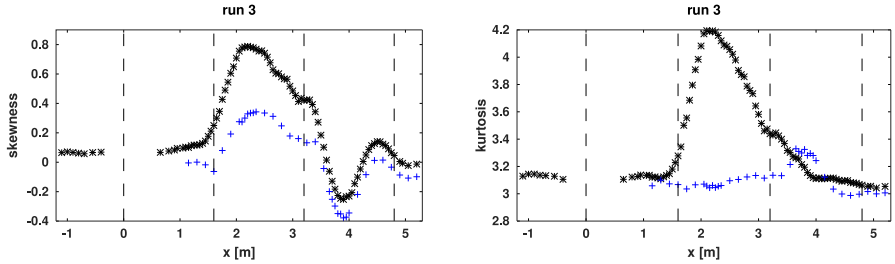

Fig. 20. Skewness (left) and kurtosis (right) of surface elevation ($*$) and horizontal velocity ($+$) from laboratory experiment [29].

5. Conclusion

We have presented a new method for calculating water particle kinematics based on surface quantities. Typical applications would be calculations of wave kinematics in surface wave models, that do not directly resolve the vertical coordinate, such as HOSM or Boussinesq-type wave models.

The proposed method calculates the kinematics by solving the Laplace equation via Dirichlet's principle with the Variational Boussinesq Model (VBM). The resulting elliptic equation is simple since the highest spatial derivatives are only of second order. The flexibility to choose the number of vertical profiles and the possibility to optimize parameters κ in Airy profiles make VBM case dependent. The parameter optimization allows VBM to obtain the best possible approximation over the relevant range of wavenumbers or wave frequencies.

The VBM has been validated extensively with Stokes waves, a nonlinear solitary wave, and irregular waves over flat bottom. In addition, we have reported laboratory experiments of regular waves propagating over a shoal with surface elevation and horizontal velocity measurements for validation. Comparison with other existing methods and laboratory experiment shows that VBM is able to efficiently solve the kinematics to high accuracy. For all the validation cases mentioned above, VBM only needs a small number of vertical profiles, typically two or three profiles are sufficient.

As an application of the developed numerical method, we have considered statistical properties of kinematics of long crested irregular waves propagating over a shoal. We show that VBM is able to capture the essential behavior of skewness and kurtosis of interior horizontal velocity reported in recent laboratory experiments [29]. Further investigation of statistical properties of wave kinematics in irregular wave fields in variable bathymetry will be reported in the future.

CRediT authorship contribution statement

Christopher Lawrence: Conceptualization, Methodology, Software, Validation, Formal analysis, Investigation, Writing, Visualization. **Odin Gramstad:** Supervision. **Karsten Trulsen:** Supervision, Project administration.

Declaration of competing interest

The authors declare that they have no known competing financial interests or personal relationships that could have appeared to influence the work reported in this paper.

Acknowledgments

The VBM is part of HAWASSI software by LabMath-Indonesia (LMI) [31]. We thank Olav Gundersen for building and installing experimental setup.

References

[1] J.C. Luke, A variational principle for a fluid with a free surface, J. Fluid Mech. 27 (1967) 395–397.
[2] V.E. Zakharov, Stability of periodic waves of finite amplitude on the surface of a deep fluid, J. Appl. Mech. Tech. Phys. 9 (1968) 190–194.
[3] L.J.F. Broer, Hamiltonian theory of surface-waves, Appl. Sci. Res. 29 (6) (1974) 430–446.
[4] J.W. Miles, On hamiltons principle for surface-waves, J. Fluid Mech. 83 (1977) 153–158.
[5] B.J. West, K.A. Brueckner, R.S. Janda, D.M. Milder, R.L. Milton, A new numerical method for surface hydrodynamics, J. Geophys. Res. 92 (C11) (1987) 11803–11824.
[6] D.G. Dommermuth, D.K.P. Yue, A high-order spectral method for the study of nonlinear gravity waves, J. Fluid Mech. 184 (1987) 267–288.
[7] W. Craig, C. Sulem, Numerical simulation of gravity waves, J. Comput. Phys. 108 (1) (1993) 73–83.
[8] W.J.D. Bateman, C. Swan, P.H. Taylor, On the efficient numerical simulation of directionally spread surface water waves, J. Comput. Phys. 174 (1) (2001) 277–305.
[9] A. Davey, K. Stewartson, On three-dimensional packets of surface waves, Proc. R. Soc. Lond. A 338 (1613) (1974) 101–110.
[10] K. Trulsen, Wave kinematics computed with the nonlinear Schrödinger method for deep water, J. Offshore Mech. Arct. Eng. 121 (2) (1999) 126–130.
[11] K. Trulsen, O.T. Gudmestad, M.G. Velarde, The nonlinear Schrödinger method for water wave kinematics on finite depth, Wave Motion 33 (4) (2001) 379–395.
[12] J.D. Fenton, M.M. Rienecker, A fourier method for solving nonlinear water-wave problems: application to solitary-wave interactions, J. Fluid Mech. 118 (1982) 411–443.
[13] W.J.D. Bateman, C. Swan, P.H. Taylor, On the calculation of the water particle kinematics arising in a directionally spread wavefield, J. Comput. Phys. 186 (1) (2003) 70–92.
[14] G. Klopman, E. van Groesen, M.W. Dingemans, A variational approach to Boussinesq modeling of fully non-linear water waves, J. Fluid Mech. 657 (2010) 36–63.
[15] G. Klopman, A Variational Approach to Boussinesq Modeling of Fully Non-Linear Water Waves (Ph.D. thesis), University of Twente, 2010.
[16] I. Lakhturov, D. Adytia, E. van Groesen, Optimized variational 1D Boussinesq modelling for broad-band waves over flat bottom, Wave Motion 49 (2012) 309–322.
[17] D. Adytia, E. van Groesen, Optimized variational 1D Boussinesq modelling of coastal waves propagating over a slope, Coast. Eng. 64 (2012) 139–150.
[18] C. Lawrence, D. Adytia, E. van Groesen, Variational Boussinesq model for strongly nonlinear dispersive waves, Wave Motion 76 (2018) 78–102.
[19] M. Gouin, G. Ducrozet, P. Ferrant, Development and validation of a non-linear spectral model for water waves over variable depth, Eur. J. Mech. B/Fluids 57 (2016) 115–128.
[20] M. Gouin, G. Ducrozet, P. Ferrant, Propagation of 3D nonlinear waves over an elliptical mound with a high-order spectral method, Eur. J. Mech. B/Fluids 63 (2017) 9–24.
[21] R. Courant, Dirichlet's Principle, Conformal Mapping, and Minimal Surfaces, Interscience, 1950, Appendix by M. Schiffer.
[22] G. Klopman, M. Dingemans, Reflection in variational models for linear water waves, Wave Motion 47 (2010) 469–489.
[23] I. Lakhturov, Optimization of Variational Boussinesq Models (Ph.D. thesis), University of Twente, 2012.
[24] J.D. Fenton, A 5th-order Stokes theory for steady waves, J. Waterw. Port Coast. Ocean Eng. 111 (2) (1985) 216–234.
[25] D. Dutykh, D. Clamond, Efficient computation of steady solitary gravity waves, Wave Motion 51 (2014) 86–99.
[26] S. Beji, J.A. Battjes, Experimental investigation of wave propagation over a bar, Coast. Eng. 19 (1993) 151–162.
[27] T. Ohyama, W. Kiota, A. Tada, Applicability of numerical models to nonlinear dispersive waves, Coast. Eng. 24 (1995) 297–313.
[28] Z.L. Zou, K.Z. Fang, Z.B. Liu, Inter-comparisons of different forms of higher-order Boussinesq equations, in: Q. Ma (Ed.), Advances in Numerical Simulation of Nonlinear Water Waves, Vol. 11, World Scientific, Singapore, 2010, pp. 287–323.
[29] K. Trulsen, A. Raustøl, S. Jorde, L.B. Rye, Extreme wave statistics of long-crested irregular waves over a shoal, J. Fluid Mech. 882 (2020) R2.
[30] L. She Liam, D. Adytia, E. van Groesen, Embedded wave generation for dispersive surface wave models, Ocean Eng. 80 (2014) 73–83.
[31] LabMath-Indonesia. Hamiltonian Wave Ship Structure Interaction (HAWASSI) software, www.hawassi.labmath-indonesia.org.